Project Title:	ECOPOTENTIAL: IMPROVING FUTURE ECOSYSTEM BENEFITS THROUGH EARTH OBSERVATIONS

Project number:	641762
Project Acronym:	ECOPOTENTIAL
Proposal full title:	IMPROVING FUTURE ECOSYSTEM BENEFITS THROUGH EARTH OBSERVATIONS
Type:	Research and innovation actions
Work program topics addressed:	SC5-16-2014: "Making Earth Observation and Monitoring Data usable for ecosystem modelling and services"

Deliverable No: 4.4

Earth-Observation Data Mining Tools

Due date of deliverable:	M30
Actual submission date:	Revised version, October 2018
Version:	V2
Main Authors:	DLR

Project ref. number	641762
Project title	ECOPOTENTIAL: IMPROVING FUTURE ECOSYSTEM BENEFITS THROUGH EARTH OBSERVATIONS

Deliverable title	EO data mining tools
Deliverable number	4.4
Deliverable version	2.0
Contractual date of delivery	M30
Actual date of delivery	Revised version, October 2018
Document status	Final
Document version	2.0
Online access	www.ecopotential-project.eu
Diffusion	Public
Nature of deliverable	Report
Workpackage	WP4
Partner responsible	DLR
Author(s)	Daniela Espinoza-Molina, Reza Bahmanyar, Octavian Dumitru, Dongyang Ao, Wei Yao, Gottfried Schwarz, and Mihai Datcu
Editor	
Approved by	
EC Project Officer	Gaëlle Le Bouler

Abstract	Deliverable D4.4 presents a number of Earth observation data mining tools used to extract information from large Image Time Series or single images and shows their evolution in time or their analyses.
Keywords	- Earth observation, multi-spectral images, SAR images, Latent Dirichlet Allocation, Data Mining, Deep Learning
	- Curonian Lagoon, Danube Delta, Doñana, Hardangervidda, and Wadden Sea

Table of Contents

1. Executive Summary

In this deliverable, we present four tools (see Table 1) to be used for extracting information from large ITS or single images together with their analyses.

- **The first tool** is called **Image Time Series - Data Mining (ITS-DM)**, which was developed for finding patterns in image archives or collections of data (*e.g..,* ITS). With this tool, we investigate the behaviour of long EO ITS in order to extract repetitive patterns and create classification maps. Moreover, this tool allows the semantic annotation of image patches and can be used with multi-spectral and SAR images.
- **The second tool** called **Latent Dirichlet Allocation (LDA)** presents a new approach for dealing with optical multi-sensor data (*e.g..,* Landsat, S-2) based on LDA used for change detection.
- **The third tool** called **Coastline Detection (CoastD)** presents a method for coastline detection using Polarimetric SAR images (*e.g.,* S-1).
- Finally, **the forth tool** called **Deep Learning (DL)** was developed to find similar patterns into an ITS collection (*e.g.,* Landsat) based on a model RNN and AutoEncoder, while the visualization tool (ITSV) was developed to help the user to visualize the ITS, to select different bands, to calculate NDVI, etc.

The data set used for evaluation of the tools is a multi-sources data set that includes the Copernicus Sentinel-1 and Sentinel-2 images and the contributing mission, Landsat images. There is one EO SAR sensor (S-1) and two EO multi-spectral sensors (S-2 and Landsat). S-1 with dual polarization was used to extract coastlines from the Danube Delta area (using **CoastD tool**) and to generate a reference dataset and classification maps of protected areas (using **ITS-DM tool**) such as the Danube Delta and the Black Sea in Romania, the Hardangervidda in Norway, and the Curonian Lagoon in Lithuania and Russia. S-2 and ITS of Landsat were used to create land cover change maps over the Doñana National Park in Spain (using **LDA tool** and **DL tool**). The Landsat ITS was kindly provided by LAST-EBD in Spain in collaboration with WP3 and WP5, and the Doñana Storyline.

This deliverable comprises the technical description of our methods, examples of application scenarios, and the developed tools.

Results of some protected areas such as Doñana and Wadden Sea are presented also in D4.2, but here the goal of the deliverable is to describe specific techniques to extract the useful information and to present this to the users. The methods are complementary with the ones presented by the other partners in WP4.

The results for Doñana National Park were validated together with Ricardo Díaz-Delgado and Javier Bustamante from Remote Sensing and GIS Laboratory (LAST-EBD), Estacion Biologica de Doñana, Sevilla, Spain, while the results for Wadden Sea were validated together with Herman Hummel and Christiaan Hummel from Department of Estuarine and Delta Studies, Royal Netherlands Institute for Sea Research (NIOZ), Yerseke, The Netherlands. The collaboration of the two institutions was in WP3, WP5, and WP9.

No.	Tool name	Methods/Algorithms/Modules	Applicable for	Data set	Test area/areas
1	**ITS-DM**	Knowledge discovery into the database and query engine with analytics	- ITS - single image	S-2 S-1	Europe Wadden Sea
2	**LDA**	Change detection based on LDA	- ITS	Landsat S-2	Bucharest Doñana
3	**CoastD**	Canny edge detector	- dual polarization	S-1	Danube Delta Hardangervidda Curonian Lagoon
4	**DL**	Recurrent neural network and AutoEncoder ITS Visualisation	- ITS	Landsat	Doñana

Table 1. The list of tools presented in D4.4.

2. Publications

In this section are listed the publications resulted from the ECOPOTENTIAL project.

1. C.O. Dumitru, G. Schwarz, and M. Datcu, "Evaluation of Retrieved Categories from a TerraSAR-X Benchmarking Data Set", IGARSS2018, Valencia, Spain, July 2018, to be published.
2. W. Yao and M. Datcu, "Deep Neural Networks Based Semantic Segmentation for Optical Time Series", IGARSS2018, Valencia, Spain, July 2018, to be published.
3. C.O Dumitru, G. Schwarz, D. Espinoza-Molina, M. Datcu, H. Hummel, and C.A. Hummel, "Analysis of Coastal Areas Using SAR Images: A Case Study of the Dutch Wadden Sea Region", book chapter in Topics in Radar Signal Processing, InTech Publishing, Rijeka, Croatia, online in May 2018.
4. C.O Dumitru, G. Schwarz, and M. Datcu, "SAR Image Land Cover Datasets for Classification Benchmarking of Temporal Changes", IEEE Journal of Selected Topics in Applied Earth Observations and Remote Sensing, 11 (5), 2018, pp. 1571-1592.
5. C.O. Dumitru, G. Schwarz, and M. Datcu, "Monitoring of Coastal Environments Using Data Mining", Knowledge Extraction and Semantic Annotation (KESA 2018), Athens, Greece, April 2018, pp. 34-39.
6. D. Ao, O. Dumitru, G. Schwarz, and M. Datcu, "Coastline Detection with Time Series of SAR Images", SPIE Remote Sensing, Warsaw, Poland, September 2017, 10422-34.
7. D. Espinoza-Molina, R. Bahmanyar, R. Diaz-Delgado, J. Bustamante, and M. Datcu, "Land-Cover Change Detection Using Local Feature Descriptors Extracted From Spectral Indices", IGARSS 2017, Fort Worth, USA, July 2017, pp. 1938-1941.
8. C.O. Dumitru, G. Schwarz, and M. Datcu, "Image Representation Alternatives for the Analysis of Satellite Image Time Series", MultiTemp 2017, Bruges, Belgium, June 2017, pp.1-4, online.
9. D. Espinoza-Molina, R. Bahmanyar, M. Datcu, R. Diaz-Delgado, and J. Bustamante, "Land-Cover Evolution Class Analysis in Image Time Series of Landsat and Sentinel-2 Based on Latent Dirichlet Allocation", MultiTemp 2017, Bruges, June 2017, pp. 1-4.
10. R. Bahmanyar, M. Datcu, O. Dumitru, D. Espinoza-Molina, G. Schwarz, C. Hummel, H. Hummel, A. Blonda, and R. Diaz-Delgado, "Analysis of Protected Areas: The Use of Satellite Images for Data Mining within ECOPOTENTIAL", WorldCover 2017, ESA-ESRIN, Italy, March 2017, online.

3. Acronyms

BoW   Bag of Words

CoastD   Coastline Detection

DMDB   Data Mining Database

DMG   Data Model Generation

EO   Earth Observation

KDD   Data Mining and Knowledge Discovery

ITS   Image Time Series

ITS-DM   Image Time Series Data Mining

LAST-EBD   Remote Sensing and GIS Laboratory

LDA   Latent Dirichlet Allocation

NDVI   Normalized Difference Vegetation Index

QEA   Query Engine and Analytics

RNN   Recurrent Neural Network

S-1   Sentinel-1

S-2   Sentinel-2

SAR   Synthetic Aperture Radar

SVM   Support Vector Machine

TRL   Technology Readiness Level

TSX   TerraSAR-X

WP   Work Package

4. Introduction

4.1 Data Mining Tools

Task 4.5 will investigate the behaviour of long time series of already pre-processed data. This includes new research with respect to quantifying habitat and ecosystem variables based on satellite data products. A priori knowledge supporting data-driven analysis will be used to generate scalable output. This will reduce the number of trivial and chance findings and visual analytical tools will be used. Time-series of data will also be analysed for feature discovery with this expected to result in the development of deep learning and/or genetic programming techniques. Two approaches will be addressed in relation to current data mining bottlenecks: supplementation of data mining with a priori domain knowledge and application of robust modelling techniques. Utilization of a priori knowledge supports data-driven analysis by making the results better scalable and by reducing the number of trivial and chance findings from data mining.

4.2 Relation of Task 4.5 with Other Work Packages and Storylines

Since the Task 4.5 (WP 4) is related to create tools for ITS exploitation it is in close relation with the Doñana Storyline, where the analysis of different land cover classes is required to estimate the changes of the vegetation over time. In addition, it includes the creation of a reference data set and classification maps of protected areas as for example: the Wadden Sea and the Dutch Delta in the Netherlands, the Danube Delta and the Black Sea in Romania, the Hardangervidda in Norway, and the Curonian Lagoon in Lithuania and Russia.

Finally, the implemented algorithm for coastal line detection shall help for a better understanding of SAR scenes used in several WPs.

4.3 Description of the Tools

In this Deliverable, we present four tools:

1. Image Time Series - Data Mining (**ITS-DM**) tool, whose goal is to find recurrent patterns in image archives or image data sets. In addition, this tool is used to semantically annotate image tiles.
2. Latent Dirichlet Allocation for multimodal ITS analysis (**LDA** tool). In this approach the goal is to analyse pairs of images to find changes and discover evolution patterns over time.
3. Coastline detection based on Polarimetric SAR data. **CoastD** tool aims at defining coastlines within SAR image data.
4. Deep Learning for Landsat ITS data. **DL** tool aims at time series data and characteristic indices selection and visualization. The visualisation tool functionalities contain the visualisation of ITS, the selection and display of different bands, the calculation of vegetation indices and the view of the curve over time.

All these tools are described in details in the next sections.

4.4 State-of-the-art *versus* Developed Tools

In [34-36] the authors showed the benefits of long-term **satellite image time series** (SITS) over 25 years in urban development and land-cover monitoring. The experiments were made on Landsat-TM SITS. In [34], they are using the spectral indices to generate temporal signatures, to define change classes in medium resolution SITS, to supervise classification of intra-annual image stacks, and to compare the results to population dynamics.

Image time series data mining tool is the first tool capable to process a large volume of data and it's allows automated image data ingestion, feature extraction, data mining based on machine learning for semantic image content annotation supported by interactive visualization tool. First version of the system was developed for TerraSAR-X images but here (in the case of ECOPOTENTIAL) can be use for EO optical or radar images (in GeoTIFF format).

Latent Dirichlet Allocation (LDA) is a statistical generative model (Bayesian), which has been introduced for discovering latent structures of collections of text documents, and represents them as mixtures of so-called topics [37]. It has been adapted and successfully applied to various image processing and computer vison problems as well as remote sensing image mining applications. The resulting topics have been shown to be usually close to the semantics that humans usually use for describing image content.

Here, we proposed a new tool for SITS analysis based on LDA. It is a three-level hierarchical model that structures the information, considering a set of latent hidden topics. This algorithms is applied to a SITS (a stack of images, each image fully covering the same area of interest) in order to obtain a land cover classification based on the temporal evolution of ground structures.

In **coastline extraction** from SAR images, in literature there are a number of publications describing different algorithms ranging from basic edge detection to polarization-based approaches [38 – 44]. Conventional methods are mainly based on amplitude SAR images and image processing approaches. As a consequence, these methods involve a lot of complicated computer processing, which is a big challenge for time series remote sensing. All these methods are not optimized for SAR images. Due to the special characteristics of radar sensors, there are many properties can be applied to accelerate the segmentation and to generate a robust algorithm.

In this idea, we introduce an automated coastline detection tool using the polarization information extracted from Sentinel-1 SAR images. By calculating a modified correlation of dual-polarimetric SAR images, the coastline can be easily, fast, and precisely obtained compared with the existing approaches.

In **RNN deep neural network**, the authors of [45] proposed to get a fixed pixel – wise semantic classification label. Later they used a sequence –to-sequence model which is able to obtain pixel –wise labels at each time. While in [46] Lichao has proposed a RNN to learn spectral-spatial-temporal features for change detection in multispectral imagery.

Facing the common problem of lacking of ground truth information for the case of SITS, we proposed to start analyzing the data with the help of domain knowledge. By using unsupervised clustering for the vegetation index along time, the data are grouped into a number of clusters. The clustered data are used as training dataset for RNN deep neural networks. In moment of the development there were very few publications investigating large SITS using deep neural networks.

5. Image Time Series – Data Mining Tool

In this chapter, we present a modular system offering Data Mining and Knowledge Discovery functionality for long time series data called Image Time Series – Data Mining (**ITS-DM**). It implements machine learning methods, image processing and database access techniques for time series content exploration and exploitation.

5.1 Description of the Tool

The **ITS-DM** tool is composed of several components: Data Model Generation (DMG), Data Mining Database (DMDB), Data Mining and Knowledge Discovery (KDD), and the Query Engine and Analytics (QEA). These components offer functionalities such as ingestion and feature extraction from radiometrically and geometrically corrected EO images, basic metadata extraction, semantic annotation of the image content based on machine learning and data mining methods, advanced querying of the image archives using metadata entries and semantic categories.

In the tool, the processing chain starts with the ingestion of EO images, followed by knowledge discovery and the data mining process to define semantic annotations for image tiles, and, finally, to enable the end-user to perform multiple queries based on different parameters and compute analytics about the data content. In the following, we describe the main components of ITS-DM.

5.2 Architecture and Processing Flow
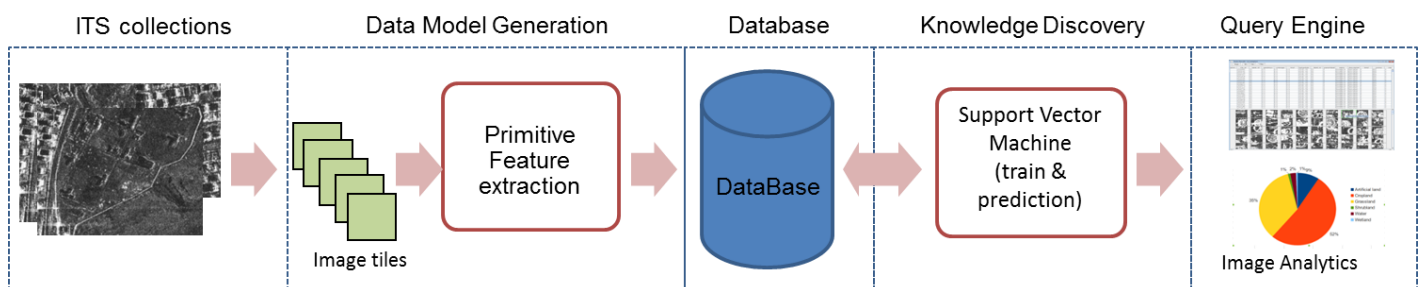
Figure1. Processing flow of the ITS-DM tool.

The main processing flow of the ITS-DM tool is presented in Figure 1. Here, the input data sources are organized in collections of images, these images are later ingested into the database via the Data Model Generation. In the following, a description of the main components is briefly presented.

5.2.1 Data Model Generation

Within DMG, the main steps performed are:

1. Metadata extraction by reading the annotation file and retrieving the relevant metadata entries as for example: locations, angles, mission information, etc.
2. Image tiling and quick-look generation in order to create a multiresolution tile pyramid (several grid levels composed of tiles with different size).
3. Feature extraction based on tiles. When applying tile-based feature extraction, the methods consider the whole patch as one entity, using the relations between all pixels within the patch and not only single pixel information. In the current version of the system, we use Gabor filters [1], Weber local descriptors [2], and colour histograms as feature extraction methods.

5.2.2   Data Mining Database

The second component: Data Mining Database is a relational Database Management System (DBMS), which acts as the core of the system, interacting with all user-oriented components and supporting their functionality. The use of a DBMS provides some advantages such as a natural integration of different kinds of information, ensuring the integrity of relationships between tables, speed of operations, etc. The database stores the information generated by the DMG component (image descriptions, metadata entries, different computed primitive features, description of tiles). The current version of the system is based on MonetDB [3].

5.2.3   Knowledge Discovery in Databases

The KDD component is used for the semantic definition of the image content. This component is based on semi-supervised learning methods and comprises relevance-feedback in order to include human expertise in the annotation process. The current version of the KDD is based on the SVM [4]-[5] algorithm. The classification is made interactively; the component shows to the user a set of image tiles to be used for the training and prediction in the SVM. Here, the operator selects a set of positive samples (images containing objects of interest) and negative samples by clicking on the tiles; thus the tiles marked in green are the positive examples, while the negative examples are marked in red. Those examples are passed to the SVM as training data. The SVM performs the prediction of the desired category based on the training data and returns the classification results. When the classification is satisfactory according to the user, the annotation of the tiles with semantic categories is stored into the database.

5.2.4   Query Engine and Analytics

The last component, the QEA [6] allows the end-user to find desired scenes and to retrieve images containing the required content and specified metadata. The image archive can be queried by using metadata and semantic definitions. In the case of queries based on given metadata, metadata entries such as geographical coordinates, acquisition angles and time, product types, etc. are used as query parameters. In the query engine it is possible to compute analytics of the query results as well as of the content of the image archive. The set of images found by the query engine can be used for further classification in the KDD module.

5.3   Examples of Experimental Results

As a first step, we ingested a collection of ten Sentinel-2 images from different places in Europa into the system using the DMG component. We cut the images into tiles of 120x120 pixels; later, we computed Weber local descriptors, Gabor filters, and colour histograms in order to be used as primitive feature descriptors. All this generated information is stored into the database.

In a second step, we performed a classification using the KDD component and human supervision. Figure 1 shows an example of image classification. This figure shows in the left-part a list of tiles and in the right-part the main image quick-look. In order to start the classification, the operator needs to select which primitive features will be used. The classification is made interactively, where the system asks for positive and negative examples (marked in green and red, respectively in Figure 1). In our example, we assumed that the operator is looking for "*Water bodies*". In a next step, the support vector machine uses these examples as training data and makes a prediction, which will result in a classification. Finally, it retrieves the classification results. In Figure 1, the tiles classified as "*Water bodies*" are marked in blue. This iterative process can be repeated several times until the operator is satisfied with the results. The number of iteration depends from user to user and also by the content of the image, but based on our experience this is around 7.
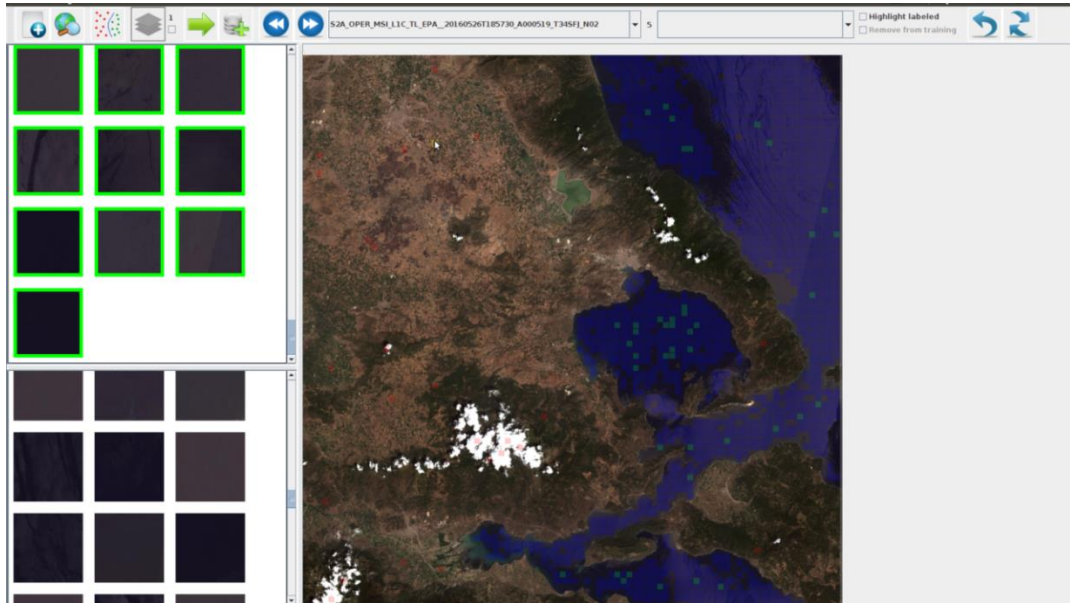
Figure 1. Classification example based on KDD: The recognized category "*Ocean*" is marked in blue.

The results of the classification can be annotated with a predefined semantic label and stored into the database. In this example, we used the label "*Ocean*" to annotate the set of tiles.

The sematic categories defined by the KDD can be used later for querying the image database. Figure 2 shows a search example based on the semantic category "*Ocean*". In this example, all the tiles annotated as "*Ocean*" are presented to the operator. The upper-part of the figure shows a list with the information of the tile such as coordinates, identifier, etc. (information extracted from the metadata of the image). The lower-part of the figure shows the quick-looks of the different tiles that were annotated and contain the "*Ocean"* category.

Similar searches can be performed using metadata parameters or a combination of metadata and semantic labels (see [13]).
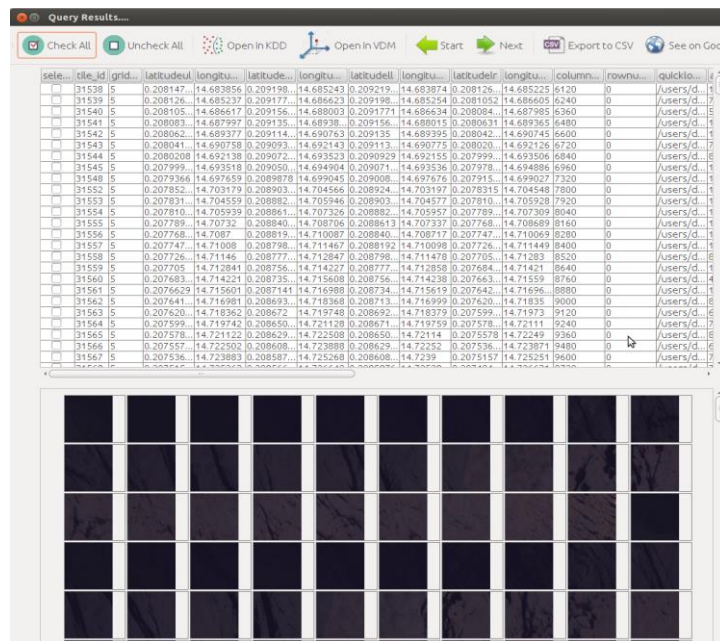

Figure 2. Search example based on the semantic category "*Ocean*".

6. Latent Dirichlet Allocation for Multimodal Analysis of ITS

In this chapter, we present a tool to analyse land cover changes and the evolution of patterns over time. This tool is based on LDA and spectral indices. LDA is a probabilistic generative model which discovers the latent structures of data collections as sets of topics [7]. In our approach, LDA is applied separately to the NDVI representation of each image to discover K topics. The topics are then used for computing the changes between the images.

6.1 Description of the Tool

We propose an approach for measuring the land-cover changes in multispectral ITS based on LDA. It considers spatial and spectral information to discover the latent image structures which are then used to compute the changes in the land-covers over time. Our approach is based on the extraction of NDVI, then the computation of BoW [21] as feature descriptors. In a next step, we apply LDA for discovering topics/changes between pairs of images. Finally, we generate change maps together with tables and plots of the average land cover changes.

6.2 Processing Flow

The processing flow of this tool is composed of the following steps (see Figure 4):

1. Computation of spectral indices and feature extraction
2. Application of LDA to the set of selected images
3. Computation of changes within a sequence of images
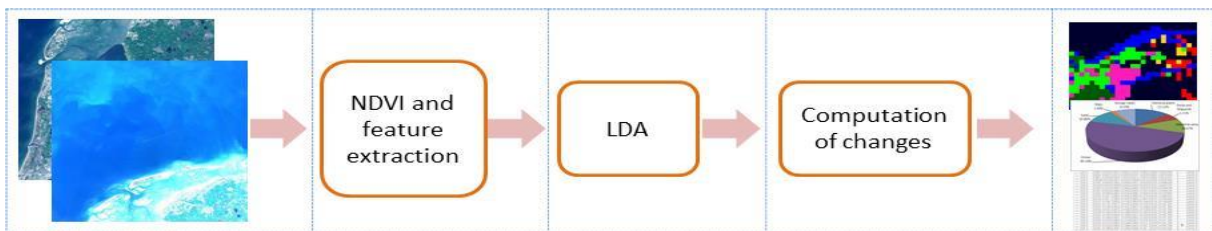4. Generation of the results (maps, tables, plots).

Figure 3. Processing flow of the LDA tool.

6.2.1 Computation of Spectral Indices and Feature Extraction

Multispectral images allow us to represent the most relevant information to every application through spectral indices, since they are combinations of spectral bands (bs) being validated based on the reflectance properties of the features of interest. In our approach, we represent the multispectral images by their Normalized Difference Vegetation Index (NDVI), a green vegetation indicator, in order to study land-cover dynamics. The NDVI can be extracted from different EO images; for Landsat images NDVI $=\frac{b4-b3}{b4+b3}$, while for Sentinel-2 images NDVI $=\frac{b8-b4}{b8+b4}$.

Figure 5Figure   shows the processing steps taking as input for the NDVI of an image and resulting in the BoW features.

The NDVI representations of the images are split into smaller patches so that the corresponding patches of the EO images (*e.g.,* Landsat or Sentinel-2) cover the same area on the ground. The patch sizes are compromises between small patches keeping the semantic analysis simple and bigger patches that are capturing the spatial context of objects. Then, we compute the local primitive features of each image patch by vectorising a neighbourhood of 3 × 3 pixels around every pixel which results in a set of nine-dimensional feature vectors. After that, for each dataset, 1% of all the computed feature vectors are randomly sampled and k-means clustering is applied to them in order to generate dictionary of N_V visual words, $V = \{v_1, v_2, \ldots, v_{N_v}\}$. The number of clusters can be empirically set to, for example, 50. The patches are then modelled as Bag-of-Words, where each *d*-th

patch of the *i*-th image is represented as sequences of N_d visual word-tokens, $W_d^i = \{w_{1d}^I, w_{2d}^I, w_{3d}^I, \ldots \ldots w_{Ndd}^I\}$ where the visual word-tokens are drawn from V.
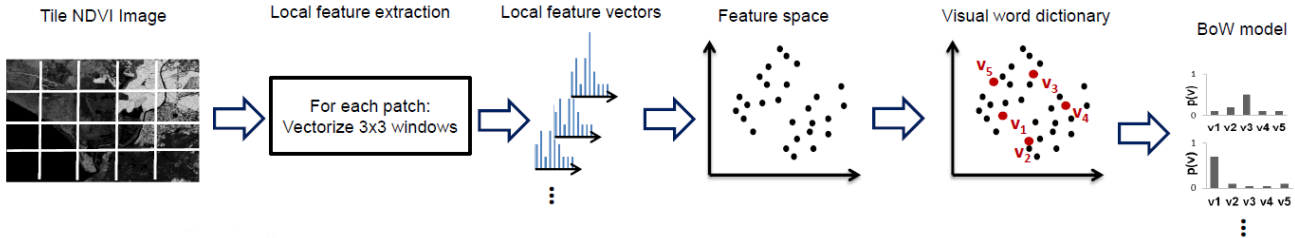

Figure 5. Computation of spectral indices and feature extraction for multispectral EO images.

6.2.2 Application of LDA to the Images

Next, LDA is applied to the BoW models in order to discover their latent structure as a set of topics; $T^i = \{t_1^i, t_2^i, \ldots, t_K^i\}$. The topics are multinomial distributions over the visual words, denoted by β^i. The distribution of the topics within each *d*-th patch is determined by a K-dimensional Dirichlet random variable θ_d^i. In order to generate each *d*-th patch of the image I_i, LDA chooses $\theta_d^i \sim Dir(\alpha)$, where α parametrizes the Dirichlet distribution. Next, for each *n*-th visual word-token, LDA samples a topic for the topic token z_{nd}^I from $Mult(\theta_d^i)$. Then a visual word is picked for w_{nd}^i from the multinomial probability distribution over the visual word dictionary conditioned on the selected topic, $p(w_{nd}^i | z_{nd}^I; \beta^i)$.

For estimating the model parameters α and β, and inferring the posterior distributions θ, LDA uses a variational Expectation Maximization algorithm [7]. Using the model parameters, the probability of each w_{nd}^I is

$$p(w_{nd}^i | \theta_d^I; \alpha; \beta^i) = p(\theta_d^I; \alpha) \sum_{z_{nd}^i} p(z_{nd}^i | \theta_d^i) p(w_{nd}^i | z_{nd}^I; \beta^I) \qquad \text{(Eq. 1)}$$

6.2.3 Computation of the Changes Using LDA

For computing the changes between a sequence of two images, the distribution of the generated words by LDA for each *d*-th patch of the earlier image (I_i), which is computed based on Equation 1, is compared to that of its corresponding patch in the later image (I_{i+1}). To this end, we assign to each image patch its most frequent topic as:

$$W_d \rightarrow t_{max} = \arg\max_j \{p(t_j | \theta_d) | p(\theta_d | \alpha)\}, j \in [1, K].$$

Then, the divergence of the topic assigned to every *d*-th patch of I_i is computed by comparing it to the corresponding patch of I_{i+1}, using Kullback-Leibler Divergence (D_{KL}) [8]. It is computed as follows:

$$D_{KL}(t_{max}^i || t_{max}^{i+1}) = \sum_{l=1}^{N_V} p(v_l | t_{max}^i) \ln \frac{p(v_l | t_{max}^i)}{p(v_l | t_{max}^{i+1})}$$

D_{KL} is not symmetric as $D_{KL}(t_{max}^i || t_{max}^{i+1}) \neq D_{KL}(t_{max}^{i+1} || t_{max}^I)$; therefore, it 14ulfils the assumption that the changes in SITS occur in chronological order.

6.3 Examples of Experimental Results

In the following experiments, we used three Landsat-5 images over Bucharest city to detect the changes between 1984 and 2011. The dataset is composed of three images acquired on 1984/21/07, 1991/19/07 and 2011/20/04; they are shown in Figure 6.

Figure 6. Landsat images over Bucharest city corresponding to (left) 1984/21/07, (middle) 1991/19/07, and (right) 2011/20/04 acquisition dates.

From a visual analysis of the test dataset, we can observe by comparing the image from 1984 with the image from 1991 that an artificial lake was created in 1991, which did not exist in 1984, in addition to some increase of the urban areas. The changes can be corroborated in the change map presented in Figure 7, which shows in red the big changes, and in blue small changes as, for example, the centre of the city (an urban area) remained constant.

Comparing the image from 1991 with the image from 2011, we can see a significant increase in the urban area, which is spreading around the centre of the city forming a kind of branches. The change map shown in the right part Figure 7Figure illustrates this aspect. Here, we can also observe that the artificial lake (created in 1991) is not appearing in red demonstrating that there is no change.
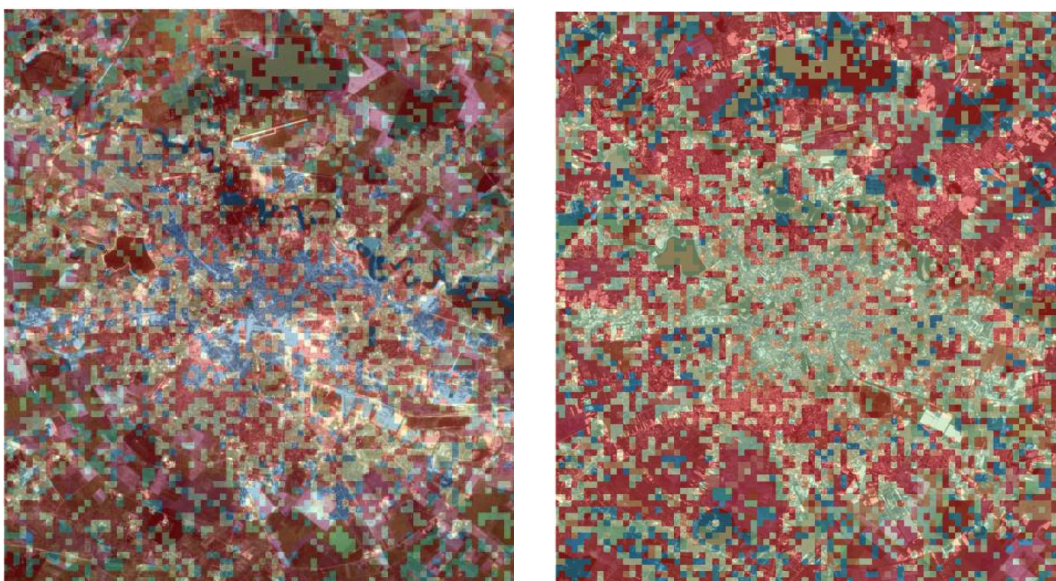
Figure 7. Change maps between images from (left) 1984 and 1991, and (right) 1991 versus 2011. Big changes are marked in red while small changes are in blue.

7. Coastline Detection based on Polarimetric SAR Data.

We present a fast and efficient coastline detection method. The experiments were run on a Sentinal-1 SAR image data set that covers the Danube Delta in Romania [9]. This method is based on a Canny edge detector.

7.1 Description of the Tool

This **CoastD** tool for coastline detection uses the polarization information that has become a popular approach to distinguish land and sea. In particular, the method described in [10] is based on a discriminating indicator which represents a modified correlation parameter and requires a cross-polarized channel. In the case of detected images, the indicator is defined for each image pixel as:

$$\gamma = \langle S_{xx} \cdot S_{xy} \rangle, \quad \text{(Eq. 2)}$$

where S are the pixel amplitudes of the polarization channels, $\{x, y\} \in \{H, V\}$, and $\langle \cdot \rangle$ stands for local ensemble averages within windows of 21×21 pixels. This indicator differs from traditional coherence. For coherence, normalization would be needed, but this step is omitted here. As a consequence, the discrepancy between land and sea becomes larger and allows easier target discrimination. The behaviour of γ over land and sea is discussed in more detail in [10] based on electromagnetic scattering models. Thus, the advantage of this polarization-based parameter is its clear distinction between land and sea targets when compared with traditional reflectivity-based metrics that do not exploit polarization effects.

The distribution of the polarimetric correlation parameter is bimodal which allows the threshold to be easily determined by its γ histogram. In this method, we use a histogram-based thresholding algorithm to find the threshold where the trough between two peaks is located. It is a simple and robust law to determine the threshold and only works if we have a bimodal histogram structure. Fortunately, the histogram of the polarimetric correlation map has a distinct minimum between two peaks.

After image binarization, the following step is to extract edges which respond to coastlines. In our case, we modified the coastline determination of [10] by employing a Canny edge detector [11] instead of a Sobel edge detector. Our Canny edge detector generates continuous coastlines. Besides, some small regions are omitted because ships on the sea may be regarded as land and the outline of the ship is not a coastline.

For time series analysis, all the images should be aligned to a master image, which is usually the first input image.

7.2 Processing Flow

In Figure 8, we present the flow chart of the coastline detection.

The methodology proposed to extract coastlines from SAR images time series contains the following steps:

1) *Data preparation*: the first step is to select the SAR image products which include coastlines and have two polarization channels (*e.g.,* VV and VH). The SAR images chosen for evaluation are Sentinel-1 images over the Danube Delta in Romania.
2) *Image alignment*: The images should be aligned to a master image. In our case, the products are already georeferenced.
3) *Correlation Calculation*: For each SAR image, Equation 2 is applied in order to extract the corresponding features. The output is a modified polarimetric–based correlation map.
4) *Histogram-thresholding*: In the correlation maps generated in step 2, a threshold is set in order to distinguish two categories, namely land and sea. This generates binary images as an output. The water bodies are represented in black and land area is represented in white.
5) *Edge Detection*: A Canny edge detector is applied to the binary images in order to extract the coastlines.
6) *Time series analysis*: The previous steps are repeated for all the images from the dataset. The variation in time is analysed combined with weather information and other factors (*e.g.,* wind, etc.).
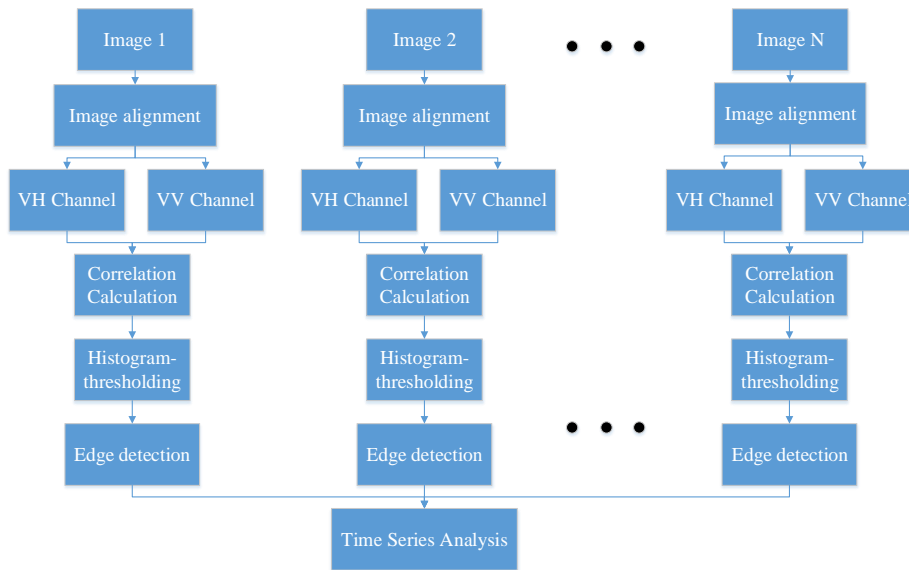
Figure 8. Processing flow for the coastline detection image time series method.

7.3 Examples of Experimental Results

Image time series refer to ordered collections of various observational records in chronological order. The purpose in this method is the analysis of SAR images time series in order to extract coastlines and change information [9]. Our test dataset is composed of four Sentinel-1 (VV and VH) scenes over the Danube delta with acquisition dates on 2016/02/22, 2016/02/24, 2016/04/12, and 2016/05/06.

In Figure 9, we display the polarimetric correlation map of a selected image from the dataset and we also show the content over the entire test site taken from Google Earth. The acquisition date of our first experiment is February 12th, 2016.

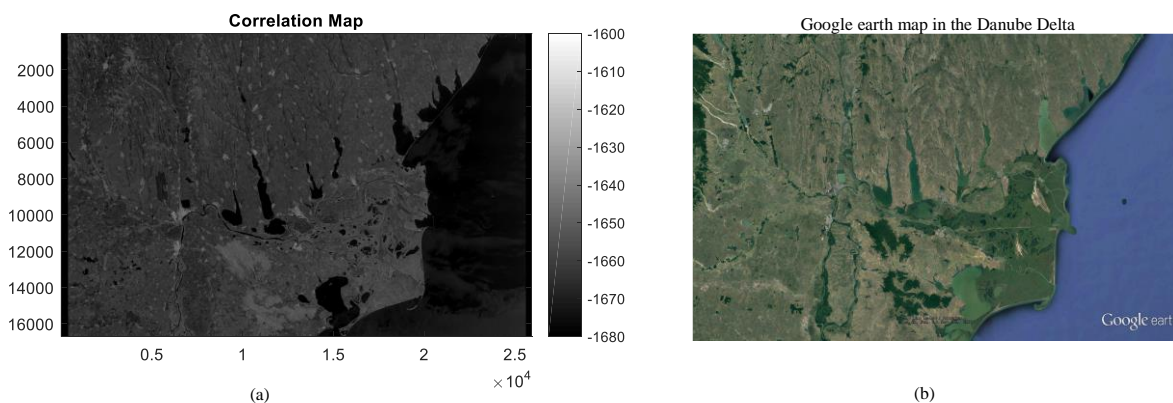**Figure 9. (a) Correlation map of the Danube Delta on February 12, 2016; (b) Location of our site on Google Earth map [12].**

The corresponding histogram and the binary image are shown in Figure 10**Figure** . The threshold used in this image is the local minimum value that separates land from sea as shown in Figure 10(a). The water bodies are represented in black and land area is represented in white.
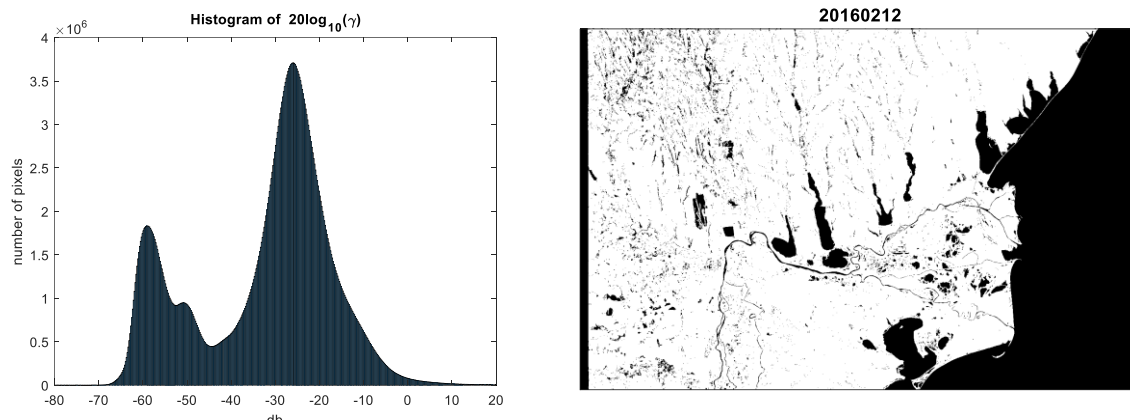
Figure 10. (a) Histogram of the correlation. (b) Binary image result.

Figure 11(a) presents the coastline extraction technique using a Canny detector for our selected area of investigation on a specific acquisition date. Figure 11(b) is a part of the full image (see Figure 11(a)) that shows a dam which delimitates the open sea from a lagoon.
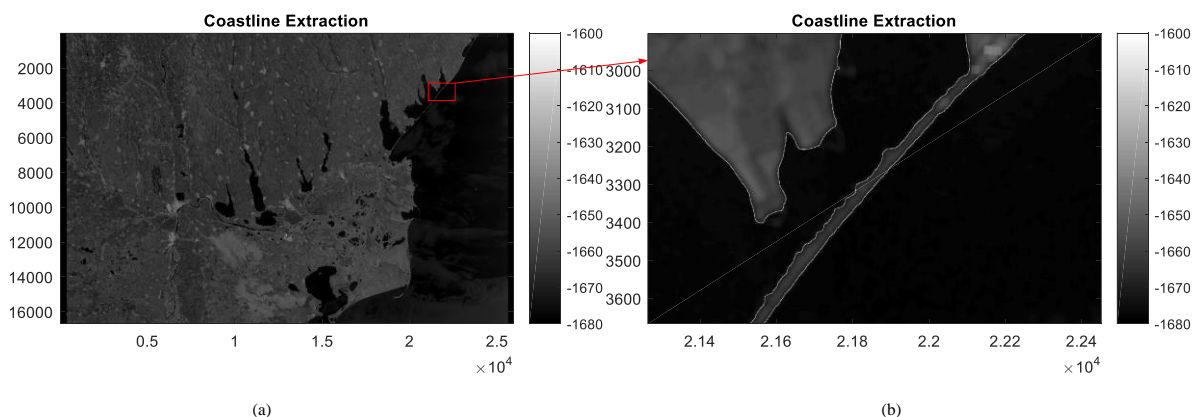
Figure 4. (a) Extracted coastlines using a Canny detector; (b) Zoomed area from the results in (a).

In the next figure, Figure 12, we show an image time series that covers the Danube Delta in Romania. Due to the large size of the SAR images, we only show the binary images.
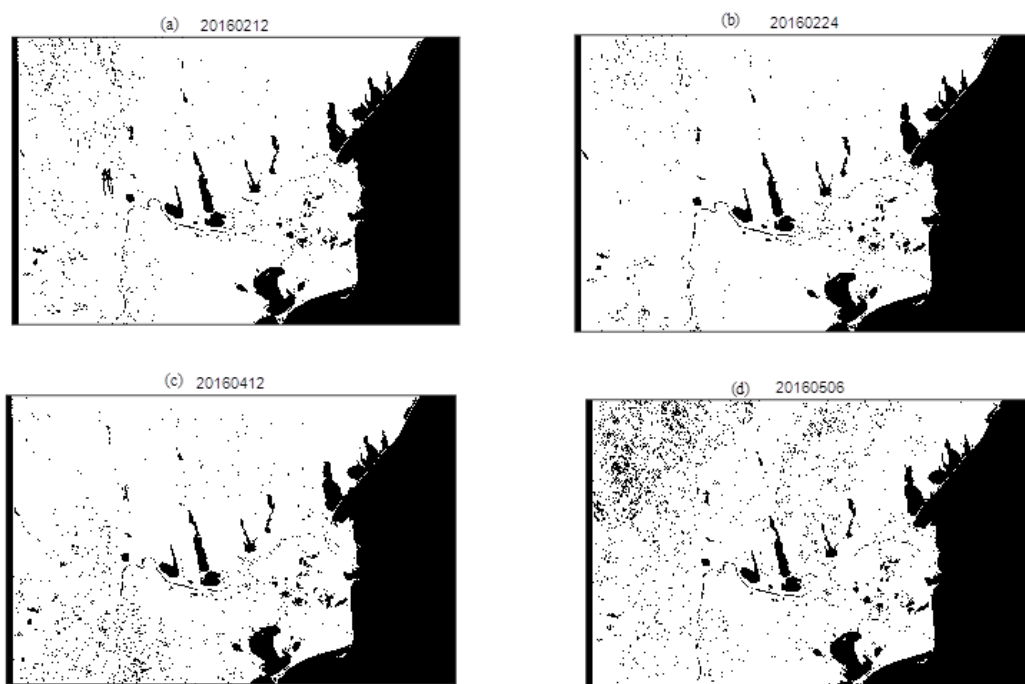
Figure 52. Binary map results (land and sea segment results) on: (a) February 12th, 2016; (b) February 24th, 2016; (c) April 12th, 2016; (d) May 6th, 2016.

8. Deep Learning for Landsat ITS Data

In this chapter, we present a tool to extract land cover temporal patterns change and the evolution of patterns over time. This tool is based on deep learning method and spectral indices.

Our dataset is Landsat products which cover the protected area of the Doñana National Park in southwestern Spain. It is an imagery time series which covers 299 scenes range from year 1999 to 2017. The Landsat SITS dataset is based on the WGS84 coordinate reference system. The images are located between the north-western coordinates (-6.905383W, 37.221228N) and the south-eastern coordinates (5.957231W, 36.76N).

8.1 Description of the Module

In our approach, we have developed a tool which visualizes the image time series, choose different bands or indices, and plot indices curves. After visualizing the image bands and indices curves, the image time series is cleaned. The cleaned time series will be prepared as training dataset, it will be put into deep learning models to learn abstract and detailed representations. A simple LSTM based Recurrent Neural Network (RNN) [27] is applied to our time series; a LSTM RNN variant model which integrates LSTM based RNN and AutoEncoder has been tested.

8.2 Processing Flow

The processing flow of the module is composed of the following steps (see Figure 13):

1. Preparation of training dataset
2. Data Observations
3. Application of LSTM model to the training dataset
4. Control of the training phases by inspecting training and testing accuracies at each iteration / each epoch.
5. Generation of the results (maps, tables, plots)
6. Generation of the intermediate representations, and check them.
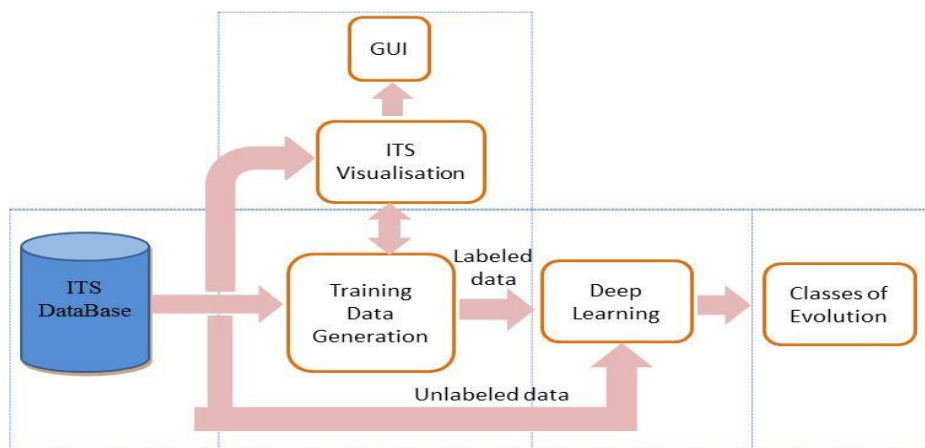

Figure 63. Processing flow of the DL tool including the visualisation of the ITS.

8.2.1 Preparation of the Training Dataset

The Landsat 5, 6, and 7 products that were analysed and consists of 6 bands: Band 1 – Blue, Band 2 – Green, Band 3 – Red, Band 4 – Near Infrared (NIR), Band 5 – Shortwave Infrared (SWIR) 1, Band 6 – Shortwave Infrared (SWIR) 2.

Data Cleaning

By viewing the RGB bands, scenes with strong artefacts, scenes with clouds, scenes are saturated were rejected for further analysis. After removing them, there are 220 scenes left.

By analysing NDVI curve, those scenes with abnormal values (e.g., very large number) are rejected.

Visualization Tool

A visualizing and analysis tool for time series has been developed (see figure 14). The functionalities contain: visualizing time series, choosing and viewing different bands, calculating vegetation indices and view the curve over time.
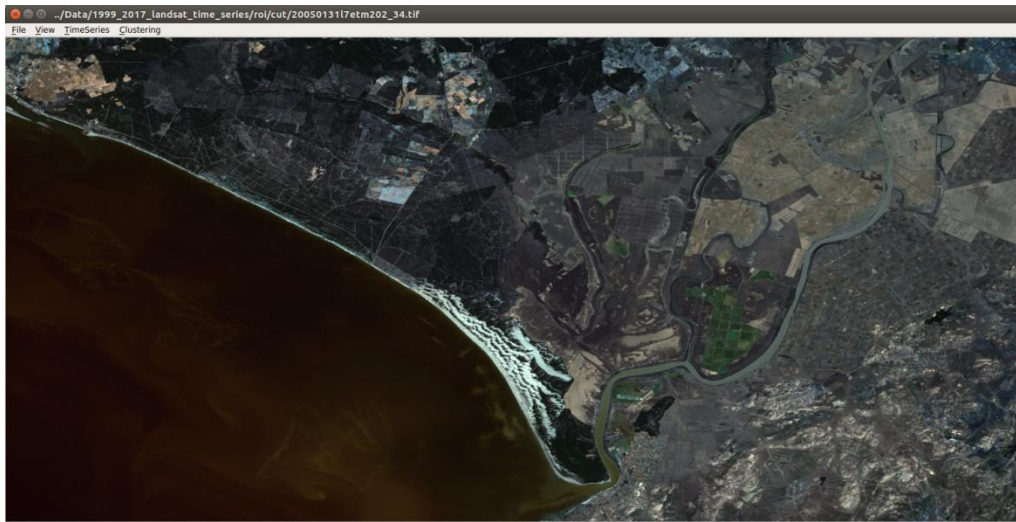
Figure 14. Visualization tool for satellite ITS.

Time Series k-Means Clustering

For each pixel location, the time series sequence is used as a data sample. All land regions and small parts of the ocean have been used as experimental data areas. After that, the data is subsampled: one data point from every 5 rows and every 5 columns. The subsampled data is taken as the input for k-Means clustering method, in order to group similar patterns together [33]. The blue band time series with a size of 1474 rows and 3030 columns have been grouped into 10 clusters.

The following figure (Figure 15) shows one example cluster and its covered mask which extracts the **paddy area** (Figure 16).

Figure 15. Cluster of NDVI time series.

Figure 16. Cluster Overlay: Paddy Areas.

8.3 Technical Description of Deep Learning Methods

As our dataset consists of 220 scenes which process time series, we use deep learning methods for the extraction of time series temporal patterns.
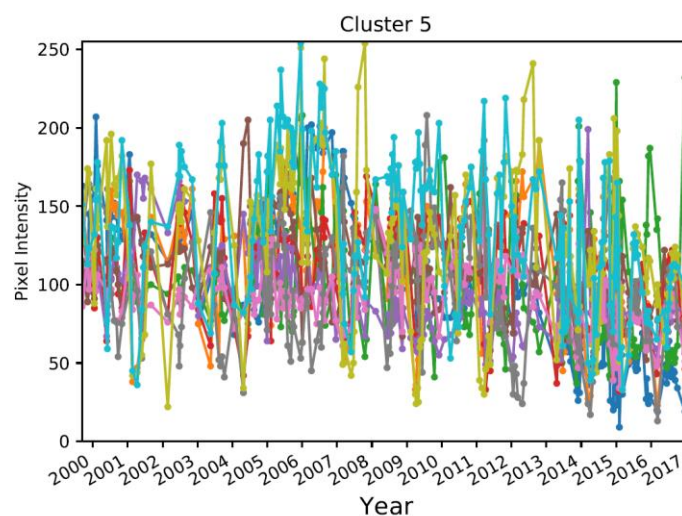
Deep learning is a group of computational models that are composed of multiple processing layers to learn representations of data with multiple levels of abstraction [27]. From bottom layers to upper layers, representations of edges, the arrangements of edges, parts of objects and objects as combinations of these parts can be learned as intermediate representations from deep neural networks.

Convolutional Neural Networks (CNN), Recurrent Neural Networks (RNN), Deep Belief Networks (DBN) are some typical models. They are widely used for image understanding, machine translation, time series prediction, etc.

As deep learning methods requires very little engineering by hand, they are very beneficial for us, aim at processing satellite imagery, by taking the advantages of applying them for the increases amount of available computation and data [30].

8.3.1 Recurrent Neural Networks (RNN)

Especially for time series, Recurrent Neural Network (RNN) is a family of neural networks which process sequential inputs, such as speech and language. RNNs process one element from an input sequence at a time, a *'state vector'* is kept in their hidden units which implicitly contains information of the history of all the past elements of the sequence [27].

Long Short Term Memory (LSTM)

With the RNNs framework, the Long Short Term Memory (LSTM) cell is proposed to overcome the long computing time problem caused by the normal recurrent backpropagation process in RNNs [28]. Hence, LSTM cell based RNNs use special hidden units which are able to keep memory for a long time. A LSTM cell consists of input gate, output gate and memory gate. Specifically, LSTM networks or GRU based RNNs are used for the encoder and decoder networks for machine translation [29].

Gated Recurrent Unit (GRU)

Gated Recurrent Unit (GRU) is a slightly variation on the LSTM. It combines the forget and input gates into a single "update gate", also merges the cell state and hidden state. GRU is simpler than standard LSTM model, and has been growing increasingly popular.

(a) An unrolled recurrent neural network. It shows the basic structure of an unrolled RNN. Each block means a chunk of neural network.	(b) RNN. It shows the basic structure of a simple RNN.
I LSTM. It shows the basic structure of a LSTM cell.	(d) GRU. It shows the basic structure of a GRU cell.

Table 2. LSTM, RNN illustration [32].

More specifically, there are four layers within a LSTM cell (see Table 3 a) to Table 3 d)).

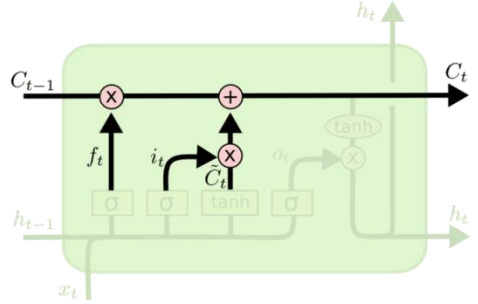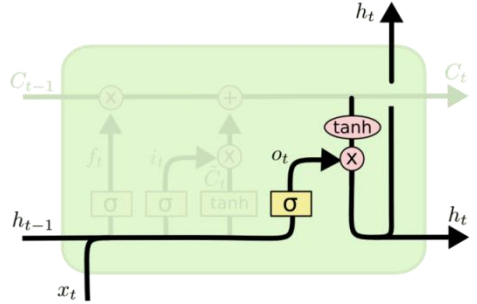|	
(a) **First Step**: a **forget gate** layer – Sigmoid function.$$f_t = \sigma\big(W_f \cdot [h_{t-1}, x_t] + b_f\big)$$	(b) **Second Step**: consists of an **input gate** layer – Sigmoid function; a tanh layer create a vector of new candidate values.$$i_t = \sigma(W_i \cdot [h_{t-1}, x_t] + b_i)$$$$\widehat{C}_t = \tanh(W_C \cdot [h_{t-1}, x_t] + b_C)$$

(c) **Third Step**: update the old cell state into the new cell state. $$C_t = f_t * C_{t-1} + i_t * \widehat{C}_t$$	(d) **Fourth Step**: consists of an **output gate** layer – Sigmoid function; a tanh layer. $$\boldsymbol{o_t} = \sigma(W_o[h_{t-1}, x_t])$$ $$h_t = o_t * \tanh(C_t)$$

Table 3. LSTM cell illustration [32].

Comparatively, a GRU consists of two layers with Sigmoid function, and one layer with tanh function (see Table 4).
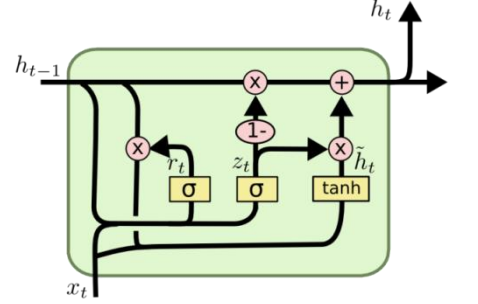
	$$z_t = \sigma(W_z \cdot [h_{t-1}, x_t])$$ $$r_t = \sigma(W_r \cdot [h_{t-1}, x_t])$$ $$\widehat{h}_t = \tanh(W \cdot [r_t * h_{t-1}, x_t])$$ $$h_t = (1 - z_t) * h_{t-1} + z_t * \widehat{h}_t$$

Table 4. GRU cell illustration [32].

Variation of LSTM: sequence-to-sequence / encoding-decoding networks

Based on LSTM, complex model can be built. For instance, sequence-to-sequence model and encoding-decoding networks are typically used in machine translation.

8.3.2   Observations

By investigating the vegetation index (NDVI) of time series Figures 17, 18, and 19, the following three kinds of time series NDVI curves patterns were noticed: repetitive pattern – paddy, sudden-change pattern – marshland, stable pattern: dune.

The left optical images show Landsat imagery at four time series index: 55, 110, 165 and 220.

The right plot shows the NDVI curve for the whole time, which ranges from the time 1 till the time 220. The x axis shows different scene number, the y axis shows the pixel intensity.

Repetitive Pattern: Paddy Areas
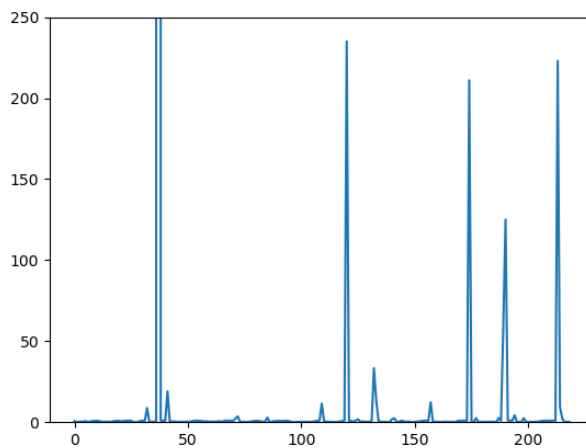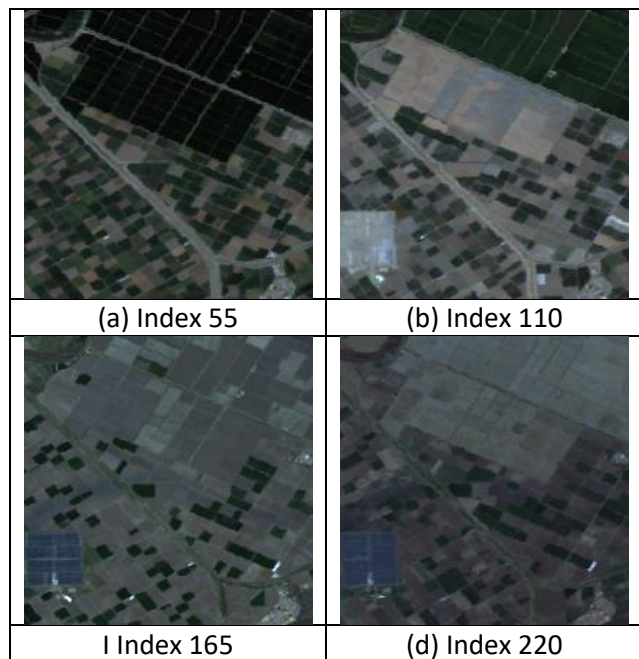
Figure 17. Time series example and NDVI curve of one location.

Sudden-change Pattern: Marshland
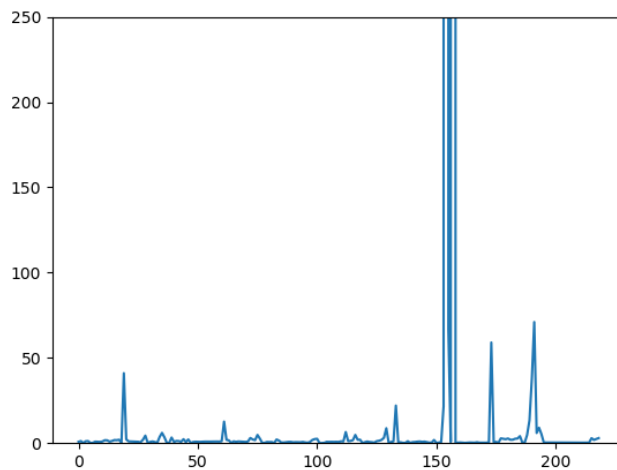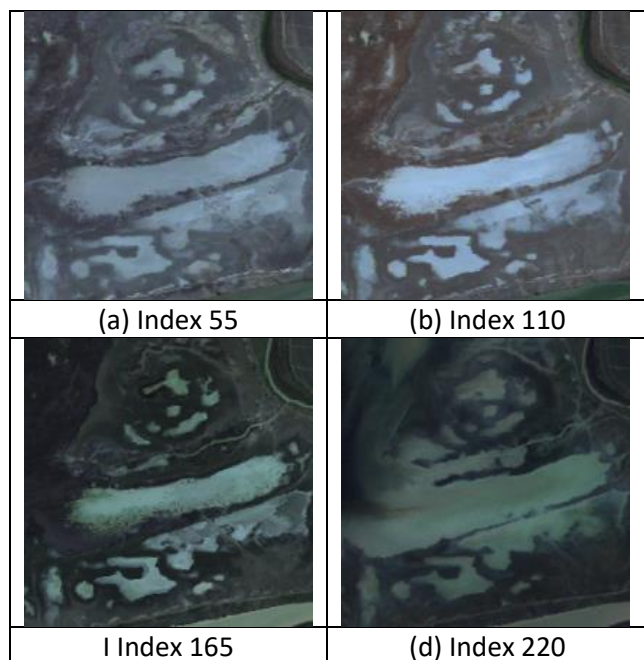
Figure 18. Time series example and NDVI curve of one location.

No-change Pattern: Dune

| (a) Index 55 | (b) Index 110 |
| I Index 165 | (d) Index 220 |
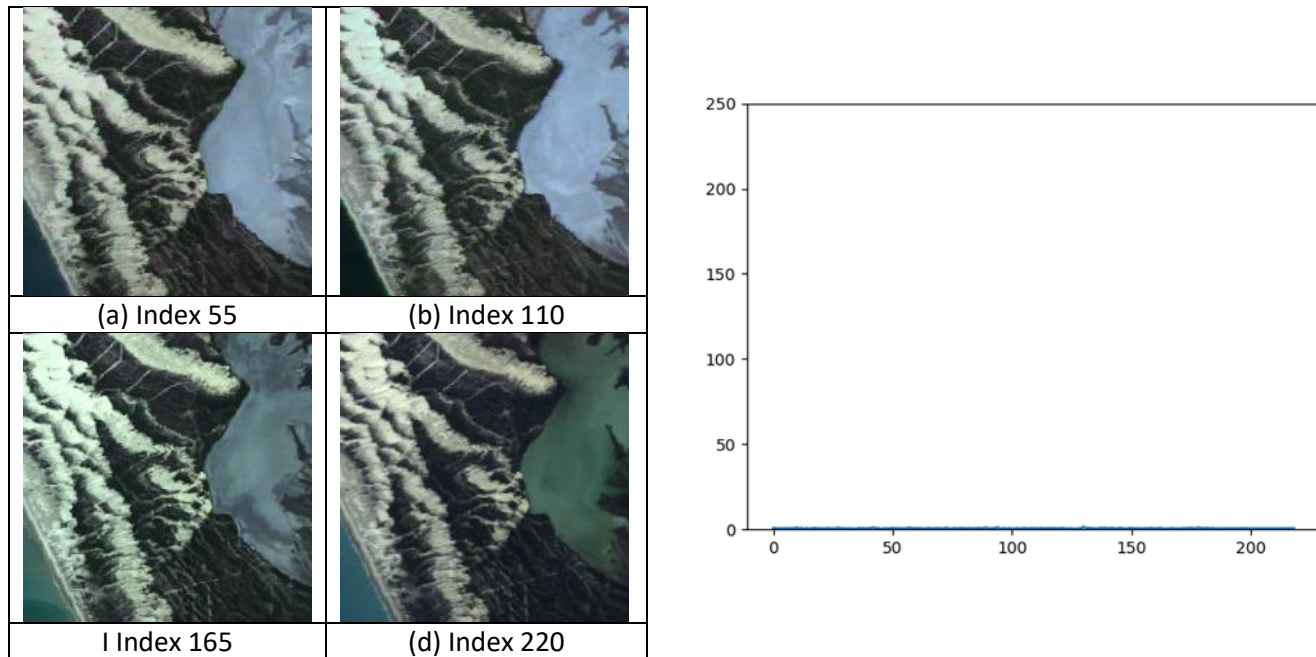
Figure 19. Time series example and NDVI curve of one location.

8.3.3   Numerical Analysis

For Landsat imagery, five different kinds of indexes can be calculated. They describe the Landsat product characteristics [31]. They are:

1. Normalized Difference Vegetation Index (NDVI)
   NDVI is calculated as a ratio between the red I and near infrared (NIR) values in traditional fashion.
   (NIR – R) / (NIR + R)

2. Enhanced Vegetation Index (EVI)
   EVI incorporates an 'L' value to adjust for canopy background, 'C' values as coefficients for atmospheric resistance, and blue band values (B). These enhancements allow for index calculation as a ratio between the R and NIR values, which reduces the background noise, atmospheric noise, and saturation in most cases.
   $$EVI = G * ((NIR – R) / (NIR + C1 * R – C2 * B + L))$$

3. Soil Adjusted Vegetation Index (SAVI)
   SAVI is calculated as a ratio between the R and NIR values with a soil brightness correction factor (L) defined as 0.5 to accommodate most land cover types.
   $$((NIR – R) / (NIR + R + L)) * (1 + L)$$

4. Modified Soil Adjusted Vegetation Index (MSAVI)
   MSAVI is calculated as a ratio between the R and NIR values with an inductive L function applied to maximize reduction of soil effects on the vegetation signal.
   $$(2 * NIR + 1 – sqrt((2 * NIR + 1)^2 – 8*(NIR-R)))/2$$

5. Normalized Difference Moisture Index (NDMI)
   NDMI is calculated as a ratio between the NIR and SWIR values in traditional fashion.
   $$(NIR + SWIR) / (NIR + SWIR)$$

T.O.5 **1 st Application of LSTM model to the training dataset**

A set of parameters need to be tuned while training the recurrent neural networks: epoch, iteration, learning rate, batch size, patch size, temporal size.

Segmentation Results

For our first preliminary experiments, we have taken 10 grouped clusters as our labels, we have performed a set of experiments with different parameter settings by using the LSTM based RNN.
Table 5 shows the first performance with different parameter settings. The best network performance with an accuracy of 40% has been achieved by networks with hyper-parameter settings {LSTM layers = 3, Cells = 64} [33].

Layers	3	3	3	3	3	5	7	10
Cells	16	32	64	96	128	32	32	32
Batch size	64	64	64	96	128	64	64	64
Accuracy	0.1171875	0.3484375	**0.4046875**	0.384343	0.378152	0.3640625	0.3375	0.36875

Table 5. The First Segmentation Results.

T.O.5 **2 nd Application of LSTM model to the training dataset**

Our second experiment results have shown great improvement, comparing to the first experiment results. We have taken 7 grouped clusters as our labels, the original full scene have been cropped into patches of size 16*16, by using a sequential recurrent encoder model.

With a 16*16 patch size, after 20 epochs, the overall segmentation accuracy has reached to around 85%.

The following illustrations are intermediate layer results over the time series for dataset with a 16*16 patch size.

Time Index 1   Time Index 50   Time Index 100   Time Index 150   Ground Truth   Prediction

Figure 20. Different time index with ground truth, and prediction.

At time index 150, convolutional RNN filter 1 the following illustrations show intermediate outputs for different gates. These filters have extracted some nearly vertical texture-like features.

Forget gate   Input gate   Output gate   Output   State

Figure 21. Intermediate outputs of specific layer with convolutional filter.

8.4   Conclusion

Facing the common problem of lacking of ground truth information, in this work, we start analysing the data with the help of domain knowledge. By using unsupervised clustering for the vegetation index along time, the data are grouped into 10 clusters. The clustered data are used as training dataset for RNN deep neural networks. An accuracy of about 40% is obtained in the first case and improved to 85% in the second case. However, the result is preliminary and a more analysis will be performed in future.

9. Application Cases Based on the Presented Tools

In order to demonstrate the usefulness of our tools for protected areas, we select some protected areas to create application scenarios than show how these tools can be applied to generate information for the management of ecosystems and protected areas. To demonstrate the feasibility of the proposed tools we are using SAR and multi-spectral data.

9.1 Generation of Reference Datasets, Classification Maps, and Statistical Analytics using the ITS-DM tool

For land cover applications, the system was used to generate a reference dataset (*i.e.,* a manually selected set of image patches with known content to be used as labelled ground truth data). This concept allows the generation of the complete processing chain as depicted in Figure 1. The results of the data analysis steps are presented in this section in various forms: as cartographic representations (*e.g.,* classification maps), as quantitative analyses, and also as accuracy figures. The results are obtained using SAR data.

In the following, we briefly explain each step of the processing chain performed to generate the mentioned results:

- *Step 1:* Select and download from a given SAR image archive images containing areas of interest.
- *Step 2*: Tile each SAR image into patches with a pre-selected size depending on the product parameters (resolution and pixel spacing) in order to cover an area of about 200×200 m on the ground. Further, generate a quick-look view of each tiled patch (in the case of Sentinel-1, these are 128×128 pixels) needed for the subsequent active learning phase.
- *Step 3*: Extract the primitive features describing each patch. We apply Gabor filters with 5 scales and 6 orientations (we compute the means and standard deviations of each coefficient; in total, we obtain 5×6×2=60 coefficients). Step1 to step 3 are performed using the Data Model Generation component of the ITS-DM system.
- *Step 4:* Classify the primitive features of each tiled patch and group them into clusters using the Knowledge Discovery in Databases component of the ITS-DM, which is based on a Support Vector Machine (SVM).
- *Step 5:* a) Initially, we have to generate correctly annotated reference data (*i.e.,* semantically labelled patches). Here we have to use SVM-based active learning starting with completely unlabelled patches. This will be completed once we have a reference dataset comprising all available categories. It can happen that some patches of our annotation images remain unlabelled. If the missing labelling creates problem cases, an expert user could help to identify the most probable category. Then the final reference datasets are visually inspected before moving to the next step. B) During routine operations, all newly arriving image patches will have to be labelled. We will assign a single most appropriate category to each patch. If no good match is found, the label *"Unclassified"* will be assigned.
  For both cases, Google Earth is used as visual support for correct labelling. For land cover SAR images, we were able to define a hierarchical semantic annotation scheme customized to high-, medium-, and low-resolution images with three levels [13].
- *Step 6:* Analyse the input datasets. First, generate classification maps of each dataset. For this a semantic classification scheme is developed and used [14]. Second, analyse the whole examined area in order to see the distribution of the retrieved categories in each image. Finally, evaluate the classification accuracy for the selected primitive features by computing characteristic metrics (e.g., precision / recall) detailing the classification results of the actual features and the reference data.

In our case, the dataset consists of medium-resolution Sentinel-1A SAR C-band data, and the image dataset covers four protected areas, namely the Wadden Sea and the Dutch Delta in the Netherlands, the Danube Delta and the Black Sea in Romania, the Hardangervidda in Norway, and the Curonian Lagoon in Lithuania and Russia. The

selected Sentinel-1A level-1 Ground Range Detected (GRD) products are High Resolution (HR) detected data taken routinely in Interferometric Wide swath (IW) mode. These data are produced (prior to geocoding) with a pixel spacing of 10×10 meters and correspond to about 5 looks and a resolution of 20×20 meters. They have a nearly uniform Signal-to-Noise Ratio (SNR) and also a stable Distributed Target Ambiguity Ratio (DTAR). The data are provided in dual polarization, VV and VH [14].

The basic finding of this section is the verification that we can perform and obtain an automated generation of classification maps and statistical analytics of SAR images, as well as quantitative performance measures.

In the next sub-sections we present the classification maps and the statistical analytics for each study case separately. Regarding the accuracy, presently we have reached a stable state of a precision/recall classification rate of 90% / 85%.

In Figure 22 to Figure 29, we show for each selected protected area and for each image the quick-look of the Sentinel-1A image, the classification map with its corresponding retrieved semantic categories, and the distribution of the identified categories. These results can give us more information about the investigated area such as "how much green area exists in the image", "how industrialized is that area", "how dense is the built-up area", "the length of the coastal area", or "green energy region (the existence of windmills)".

An interesting phenomenon that that we have identified as a result of image analysis and semantic annotation is that for medium-resolution images (e.g., Sentinel-1 data) the number of the identified semantic categories is lower and are general categories (e.g., Inhabited built-up areas) than for high-resolution images (e.g., TerraSAR-X data) where we obtain more categories with more details (e.g., *Medium-density residential areas*) [15].

In the case of image time series (e.g., natural disaster applications), these classification maps can be used to inspect the temporal evolution of the affected areas and to analyse the whole examined area in order to detect any changes (e.g., in the case of a disaster).

9.1.1   The Curonian Lagoon, the Danube Delta, the Hardangervidda, and the Wadden Sea

In the next figures, Figure 22 to 29, we show the classification maps and the distribution of categories for different Sentinel-1 images that cover four ECOPOTENTIAL protected areas, namely the Curonian lagoon, the Danube Delta, the Hardangervidda, and the Wadden Sea [24] and their surrounding areas.

For the Wadden Sea area, we compare the results (e.g., classification maps and the distribution of categories) obtained using Sentinel-1 data with the results using TerraSAR-X data [23]. An interesting phenomenon is the higher number of categories found for the TerraSAR-X images compared to Sentinel-1A. Typically, the total number of categories that can be identified in a high-resolution SAR image (e.g., TerraSAR-X data) varies from 10 to 20 categories depending on the content of the image, while in the case of medium-resolution SAR images (e.g., Sentinel-1 data) the total number of categories varies from 6 to 15. This phenomenon can be explained by a greater discrepancy between the (visually hidden) feature vectors, and by the architectural and geographical location of these images.

Some of these categories contain a small number of patches (less than 1% from the entire number of patches) and other categories contain a large number of patches (more than 40% from the entire number of patches). This depends on the data coverage. Usually, the main categories (in or case) are *Sea* and *Agricultural land*, while the categories with a small number of patches (in our case) are *Boats, Airport runways, Bridges, Harbour infrastructures*, etc. For example, for the first case, in Figure 23 the *Sea* category represents about 49%; in Figure 25 the *Agricultural land* category represents 52%; in Figure 27 the *Sea / Channel* category represents 51%; and in Figure 29 the *Agricultural land* category represents 41%. In the second case, these categories represent less than 1%, in Figure 23 the *Airport runways, Boats, Harbour infrastructures,* and *Storage tanks* categories; in Figure 25 the *Bridges*, *Irrigated areas*, *Flooded areas*, and *Sandbanks/Beaches* categories; in Figure 27 the B*oats* and *Islands* categories; and in Figure 29 the *Airport runways, Boats, Bridges, Channels, Firth,* and *Harbour infrastructures*.

Another phenomenon [24] to be mentioned are the detailed semantic categories that are obtained in the case of TerraSAR-X (e.g., *Medium-density residential areas*, *Mixed forest*, etc.) in contrast to the categories in the case of Sentinel-1A (e.g., *Inhabited built-up areas*, *Natural vegetation*, etc.).

Presently, we have reached a stable state of classification accuracy (a precision/recall [25]) rate of 90% / 85% for Sentinel-1A.

Legend:
- *Airports runways*
- *Black edge (image edge effect)*
- *Boats*
- *Channels*
- *Coastal areas*
- *Harbor infrastructures*
- *Lakes*
- *Inhabited built-up areas*
- *Mixed forest*
- *Sand banks / Dicks*
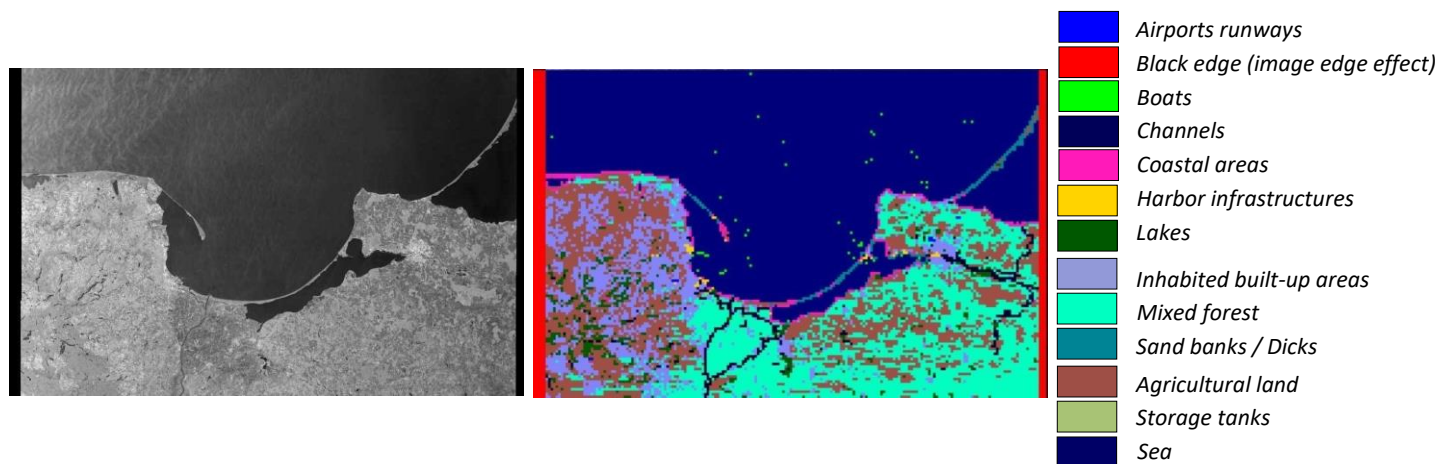- *Agricultural land*
- *Storage tanks*
- *Sea*

Figure 22. Sentinel-1 quick-look view (left) and the "patch-based" classification map (right) for an image of the Curonian Lagoon, Lithuania / Russia [14].
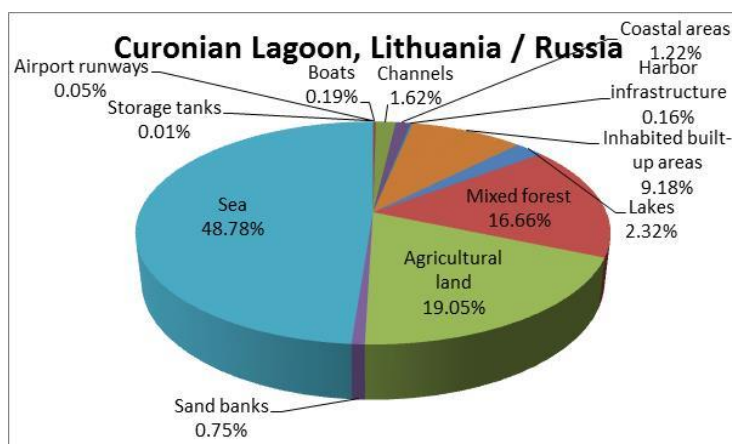

Figure 23. Diversity of categories identified from single images of the Curonian Lagoon [14].
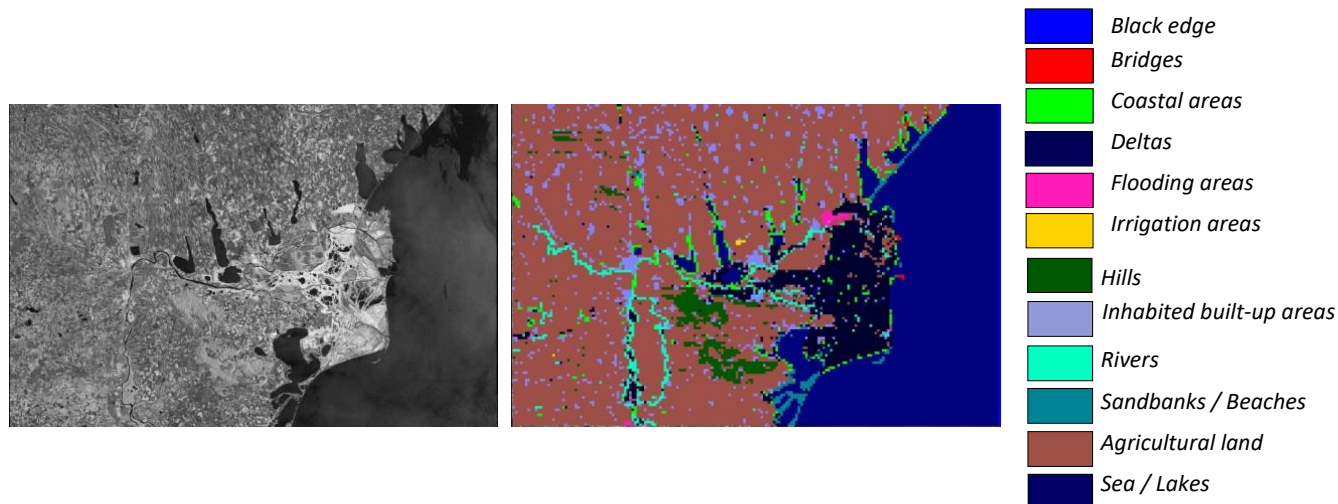
Legend:
- Black edge (blue)
- Bridges (red)
- Coastal areas (green)
- Deltas (dark blue)
- Flooding areas (magenta)
- Irrigation areas (yellow)
- Hills (dark green)
- Inhabited built-up areas (light purple)
- Rivers (cyan)
- Sandbanks / Beaches (teal)
- Agricultural land (brown)
- Sea / Lakes (navy)

Figure 24. Sentinel-1 quick-look view (left) and the "patch-based" classification map (right) for an image of the Danube Delta, Romania [14].

Figure 25. Diversity of categories identified from single images of the Danube Delta [14].

Legend:
- Black edge (blue)
- Boats (red)
- Coastal areas (green)
- Islands (dark blue)
- Mountains (magenta)
- Sea / Channels (yellow)

Figure 26. Sentinel-1 quick-look view (left) and the "patch-based" classification map (right) for an image of the Hardangervidda, Norway [14].
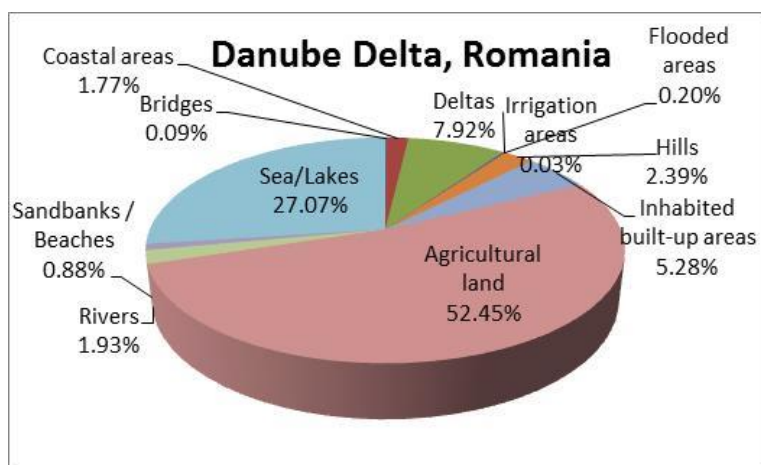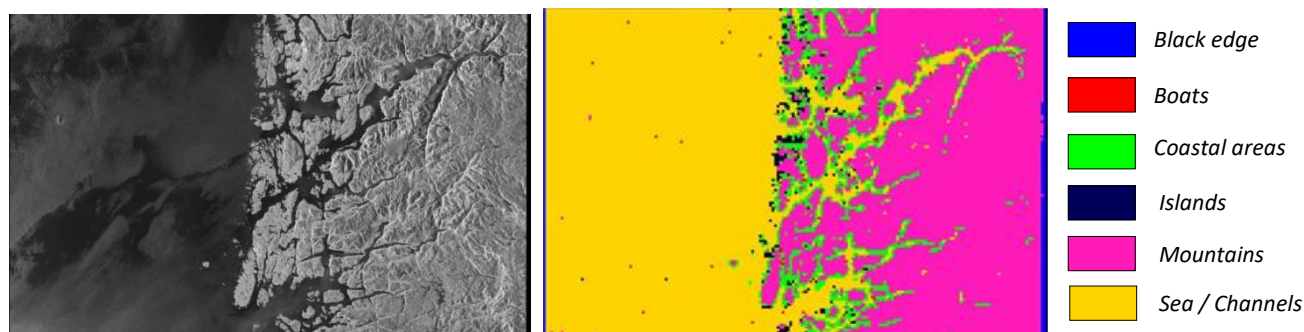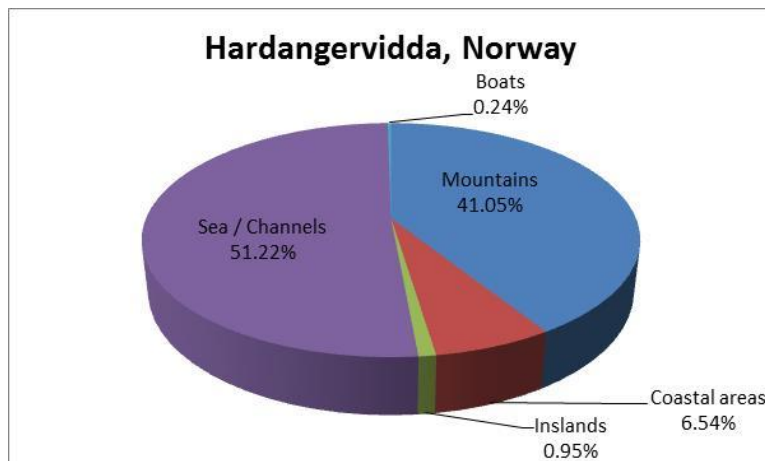
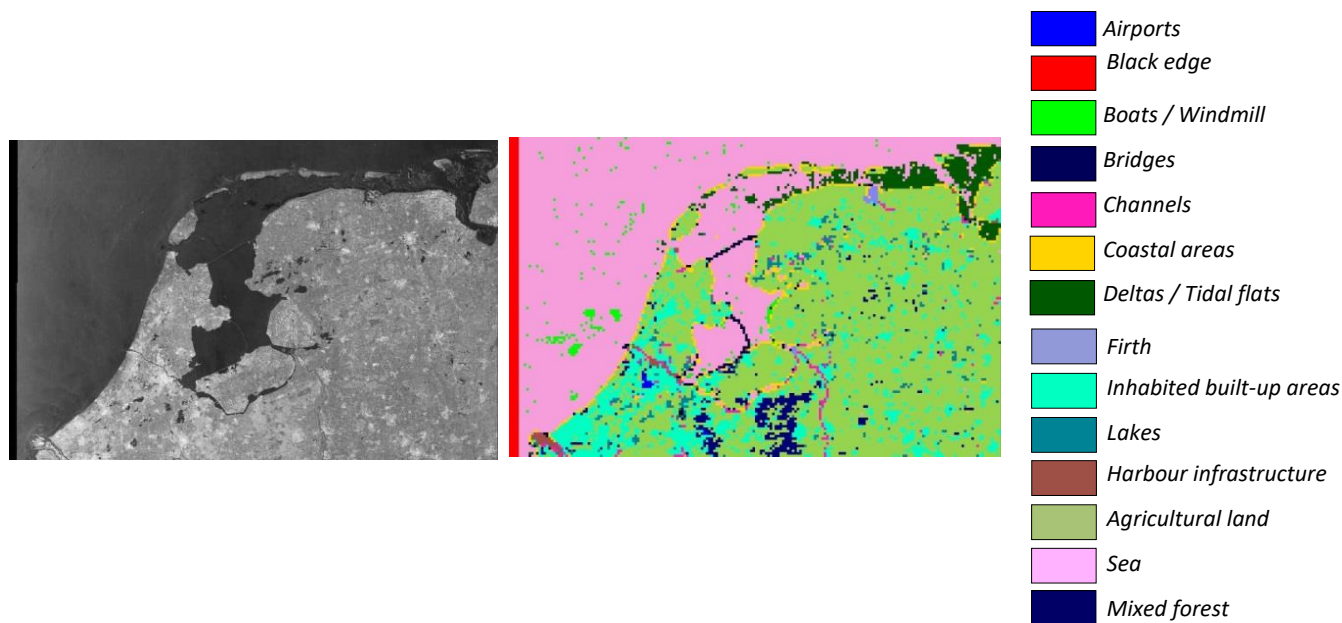**Figure 27. Diversity of categories identified from single images of the Hardangervidda [14].**

Figure 28. Sentinel-1 quick-look view (left) and the "patch-based" classification map (right) for an image of the Wadden Sea, the Netherlands [14].
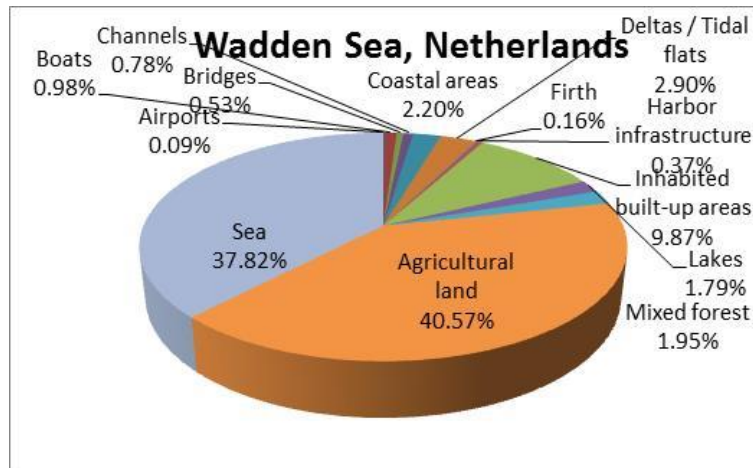
Figure 29. Diversity of categories identified from single images of the Wadden Sea [14].

9.2 Land Cover Change Detection Based on Spectral Indices and LDA

9.2.1 Doñana National Park as a Study Zone

The study zone for the next two applications is the protected area of the Doñana National Park in southwestern Spain. The Doñana marshes are considered as the largest sanctuary for migratory birds in Western Europe. Therefore, monitoring its land-cover changes is in high demand by decision-makers for an effective management of the park [16], [17]. The Landsat and Sentinel-2 SITS datasets used in our application cases are both based on the WGS84 coordinate reference system. The images are located between the north-western coordinates (-6.905383W, 37.221228N) and the south-eastern coordinates (5.957231W, 36.76N). Figure 30 shows the location of the study zone and an RGB composite of one image. The Landsat Image Time Series data set was provided by LAST-EBD [26].
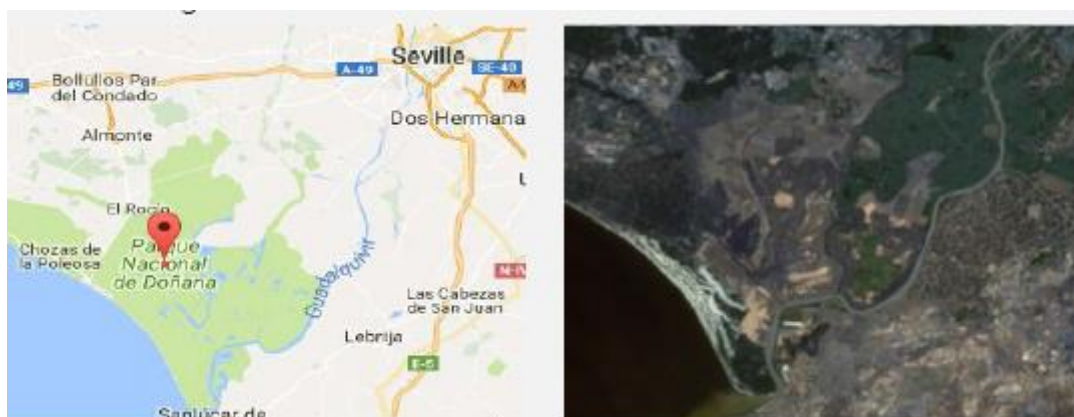
Figure 30. (Left) Location of the study zone. (Right) RGB composite of a Landsat-5 image.

In the following, we present two applications. The first one is extracting changes based on spectral indices and clustering methods (i.e. k-means) to generate change maps. The full description of this work is presented in [22]. The second application uses a larger data set of EO images (Landsat and Sentinel-2) to discover the evolution of patterns over time. Here the changes are computed between pairs of images by applying an LDA method. The full version of this work is presented in [23].

9.2.2   Land Cover Change Detection Using Local Feature Descriptors Extracted from Spectral Indices

Our test dataset is composed of a collection of six Landsat-5 images acquired every other month from October 2009 to August 2010.

In this example, a multispectral SITS dataset is used for detecting land-cover changes (e.g., vegetation and water bodies) which can be applied to ecosystem monitoring. Therefore, we employ three relevant indices, namely the Normalized Difference Vegetation Index (NDVI), a green vegetation indicator, and two variations of the Normalized Difference Water Index (NDWI) related to liquid water. While NDVI represents the water content of the green leaves, NDWIb indicates the water levels of the water bodies. In our approach, each multispectral image is represented by the three index bands. In order to discover the existing land-cover classes, local image features are represented in two different ways:

- Each pixel is described by a vector of its indices resulting in a three-dimensional vector.
- For each pixel, a local neighbourhood of 3x3 pixels is vectorised on every index band.
- The resulting vectors are then concatenated to form a vector of 27 elements.
- The resulting feature vectors then form a multidimensional Euclidean space, the so-called feature space. After that, for each image feature representation,
- 30% of all local feature vectors (all the six given images are considered together) are randomly sampled and a clustering method (e.g., k-means) is applied to them.
- The resulting clusters are assumed to represent the existing land-cover classes.
- Finally, the rest of the local feature vectors are assigned to their closest clusters resulting in classifications of the images.

9.2.2.1 Experimental Results and Discussion

We applied k-means to our SITS dataset represented by feature vectors computed based on the spectral pixel index values and on the local pixel neighbourhoods on spectral indices. In our experiments, the number of clusters is set to 10 based on a scientific estimation of the existing main land cover classes [22].

Figure 31 demonstrates the land-cover classification of the Doñana protected area from October 2009 to August 2010 with two month intervals. Figure 32(b) represents the change dynamics measured between consecutive image pairs for the annotated land-cover classes in Figure 32(a). It can be observed that:

- From **October to February**, the amount of sediment carried by the river to the ocean is increasing which influences the ocean water turbidity.
- During **spring and summer**, the amount of sediment brought to the ocean by the river decreases.
- Between **December and February**, marshlands were flooded and therefore, Figure 32(b) shows a significant change in this period which is consistent with the flooding cycle of the region reported in [18].
- In **April**, the flood water started draining and various land-cover classes appeared (e.g., *Shallow and mid-level water*, *Bushes*) in the affected regions.
- Between **April and June**, the next large change occurred; see Figure 32(a), when the water mostly drained. The land-cover in this area only slightly changed during summer.
- For **the rice paddies**, according to Figure 32(b), the most significant change occurred between April and June when rice plants appeared in the paddies (refer to Figure 31) which is consistent with the rice plantation cycle. The plants continued growing through summer; however, their change was not significant.
- In the **berry fields**, the considerable changes occur in spring and summer when the plants grew in the region.
- The **dune area** experienced a notable change between December and February; see Figure 32(b). As shown by Figure 31, this change refers to the disappearing of the sparse vegetation in the area.
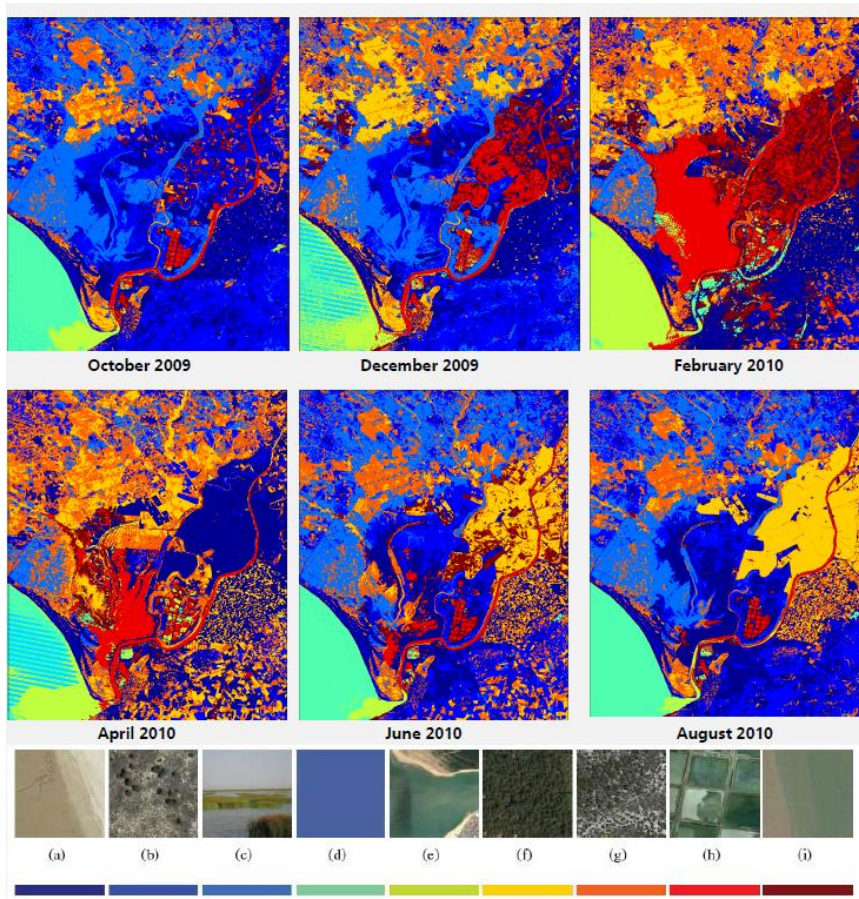
Figure 31. Land-cover classification of the Doñana protected area from October 2009 to August 2010 with two month intervals. The legend represents (a) *Bare soil*, **(b)** *Very sparse vegetation*, **(c)** *Marshland*, **(d)** *Deep water* such as *Ocean*, **I** *Sediment*, **(f)** *Forest*, **(g)** *Bushes*, **(h)** *Mid-level water*, **(i)** *Shallow water*.

Figure 32. (a) Manual annotations of four land-cover classes of interest. (b) Change dynamics measured between consecutive image pairs for the annotated land-cover classes in (a).

Figure 33 shows the change-map created for the results presented in Figure 31 as well as the average change computed for the four land-cover classes of interest. As the map and the table show, the land-cover changes mostly occur in the regions affected by the flooding and in the regions where we experience seasonal vegetation changes such as agricultural fields. Moreover, the big changes in the ocean are due to artifacts in the images.
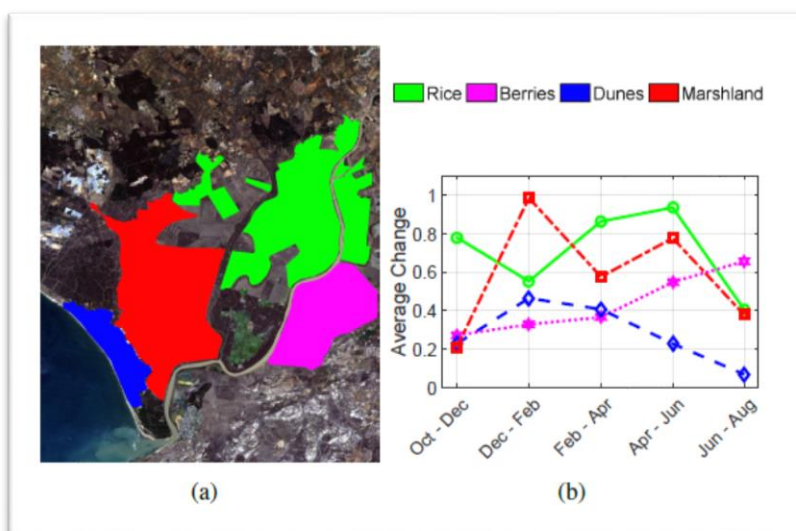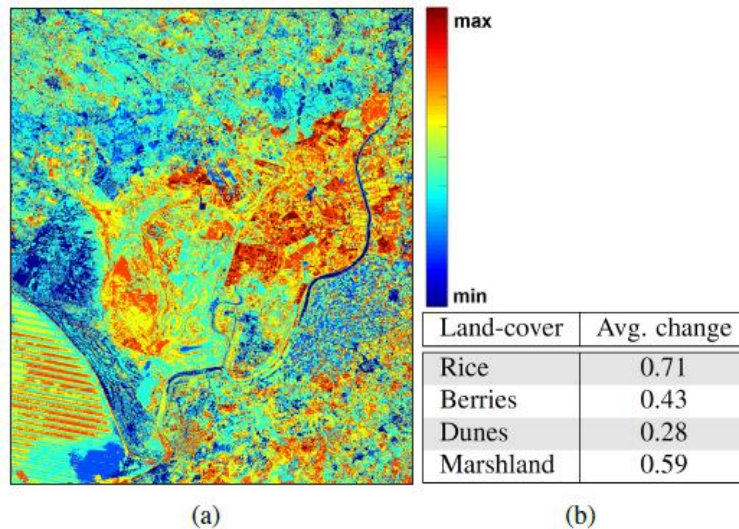

Land-cover	Avg. change
Rice	0.71
Berries	0.43
Dunes	0.28
Marshland	0.59

(a) (b)

Figure 33. (a) Land-cover change-map. (b) Average changes computed for the annotated land-cover classes.

9.2.2.2 Conclusion

In this research work, we quantitatively and qualitatively assessed the land-cover changes in the Doñana protected area using a SITS dataset generated from Landsat-5 satellite images captured every second month from October 2009 to August 2010. To visualize the changes, the images are represented by spectral indices. Then each image pixel is described by a vector of the index values of its neighbours (i.e., feature vectors). After that, the land-cover classes are discovered by applying k-means clustering to the feature vectors. The change in a point is then measured as the number of times the assigned land-cover class to the point changes over time. Our results show that computing local descriptors from the index representation of the images allows us to discover more homogeneous land-cover classes, compared to the direct use of the spectral index values. These classes can be further used to assess the land-cover dynamics over time and the affecting parameters. Due to the low temporal resolution of our test dataset, only coarse changes could be detected; however, for a finer change dynamic analysis, a higher temporal resolution is suggested to be considered as a future activity.

9.2.3   Land-Cover Evolution Class Analysis in ITS of Landsat and Sentinel-2 Based on LDA

The complete description of this study is presented in [23]. For this application we used Landsat images and Sentinel-2 images; our Landsat dataset is composed of 18 multispectral images (nine Landsat-5 and nine Landsat-7 images), of 3030×1474 pixels (the bands with 30 m spatial resolution), acquired between September 2009 and August 2010. The Sentinel-2 dataset contains 14 multispectral images of 9362×4554 pixels (the bands with 10 m spatial resolution), acquired from December 2015 to December 2016. Both datasets cover periods of one year allowing the study of seasonal land-cover changes.

9.2.3.1 Experimental Results and Discussion

Throughout our experiments, we address vegetation changes of three significant land-cover classes including two types of irrigated agriculture fields (*Rice* and *Berries*) and *Marshlands*. In order to analyse the change dynamics for these land-cover classes, a ground truth annotation was manually generated based on the information provided in [16], [17] and [19], which is shown in Figure 34.

Figure 34. Manual annotation of the land-cover target classes.

The results were then validated based on the previous studies of land-cover changes in the Doñana National Park [16], [17], and [19]. Moreover, the results were qualitatively evaluated by a group of experts from LAST-EBD [26], knowledgeable about the land-cover of the Doñana National Park.

Index	Landsat (2009/2010)	Sentinel-2 (2015/2016)
1	23 Sept – 09 Oct	01 Dec – 12 Dec
2	09 Oct – 02 Nov	12 Dec – 09 Mar
3	02 Nov – 04 Dec	09 Mar – 08 Apr
4	04 Dec – 29 Jan	08 Apr – 22 May
5	29 Jan – 06 Feb	22 May – 07 Jun
6	06 Feb – 03 Apr	07 Jun – 06 Jul
7	03 Apr – 27 Apr	06 Jul – 20 Jul
8	27 Apr – 05 May	20 Jul – 26 Jul
9	05 May – 21 May	26 Jul – 08 Aug
10	21 May – 06 Jun	08 Aug – 05 Sept
11	06 Jun – 22 Jun	05 Sept – 04 Oct
12	22 Jun – 30 Jun	–
13	30 Jun – 16 Jul	–
14	16 Jul – 01 Aug	–
15	01 Aug – 25 Aug	–

Table 6: Time intervals corresponding to the indices of the plots in Figure 33 and Figure 34

Figure35 and Figure 36 demonstrate the vegetation change dynamics for the three land-cover classes, while Table 6 depicts the time intervals in which the changes were measured. Figure 35(a) and (b) represent the computed change as D_{KL} for the Landsat and Sentinel-2 datasets, respectively. In order to be comparable, the results were normalized by the time intervals. According to Figure 29, the marshlands experience a significant change during winter (04 Dec – 06 Feb) which is due to flooding. This is consistent with the flooding cycle of the region reported in [18]. Comparing to the results obtained from the Landsat dataset, the Sentinel-2 dataset does not show a

considerable change in marshlands. According to [20], in 2015/2016, when the Sentinel-2 images were acquired, the area was fully covered by flood water and the region experienced a dryer year as compared to 2009/2010 when the Landsat images were taken. Therefore, the range of the vegetation dynamics in 2009/2010 was larger than in 2015/2016. Figure 36 shows the change dynamics for the target classes as the differences between NDVI values of consecutive images (blue curves) versus the change dynamics computed based on our approach (red curves). The first and second rows present the results based on the Landsat and Sentinel-2 datasets, respectively. The figure demonstrates that the change dynamics computed by our approach has similar patterns as the NDVI does in the most cases.
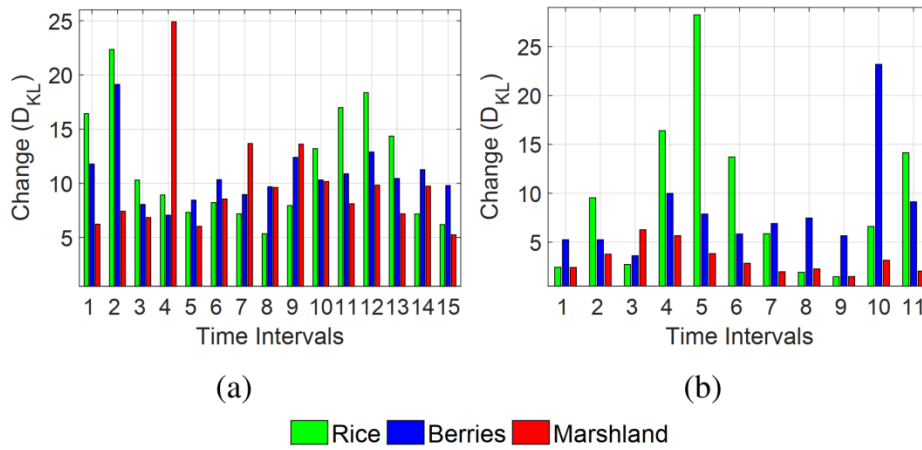
Figure 35. Changes computed based on the (a) Landsat and (b) Sentinel-2 datasets for the three target land-cover classes. The time intervals are depicted in Table .
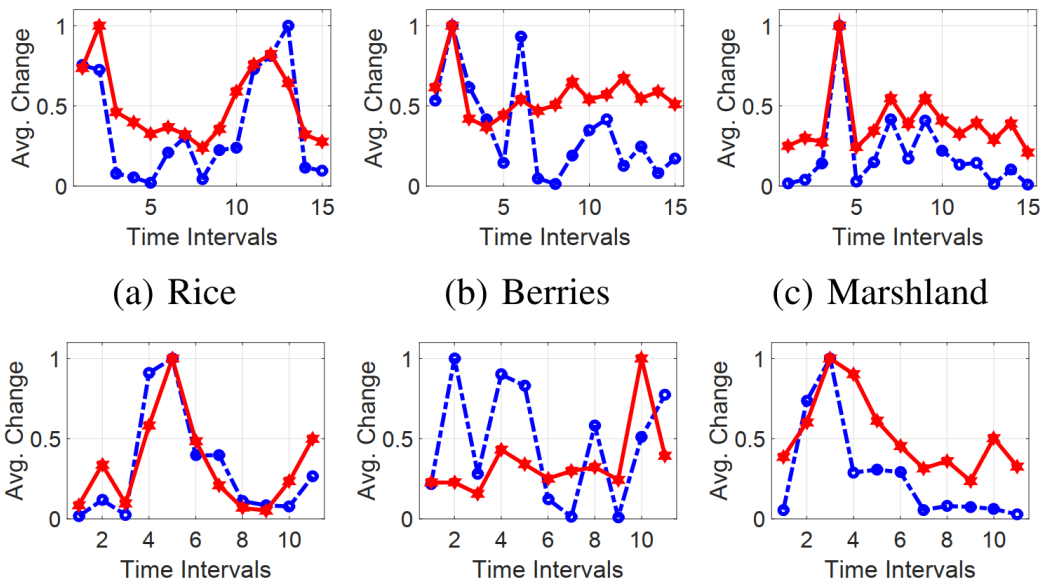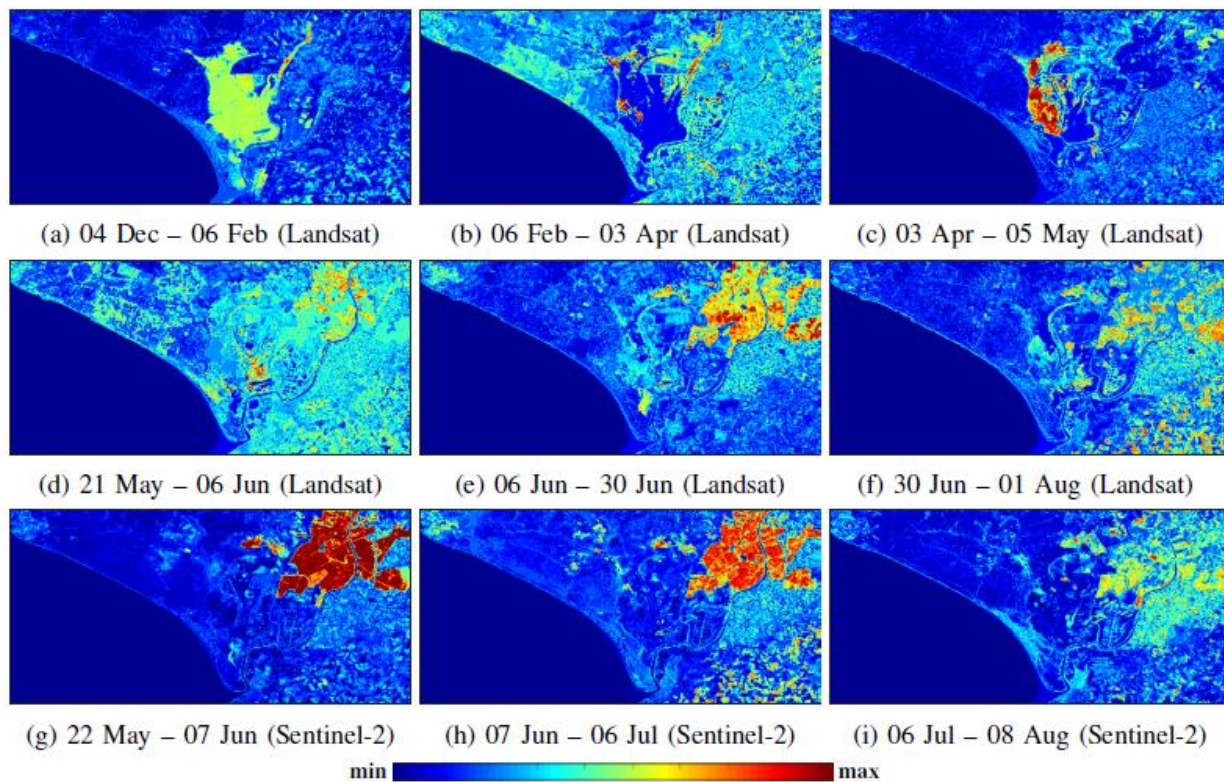

Figure 36. Change dynamics as the differences between NDVI values (blue curves) versus the change dynamics based on our approach (red curves). (a–c) and (d–f) present the results based on the Landsat and Sentinel-2 datasets, respectively. The time intervals are depicted in Table .

Figure 37. Demonstration of the vegetation changes computed by our proposed method. (a–c) in marshlands between December and May based on Landsat, (d–f) in rice fields between May and August based on Landsat, and (g–i) based on Sentinel-2.

Figure 37 visualizes examples of the vegetation changes computed by our approach. According to Figure 36(d), large changes in marshlands occurred between 04 Dec and 06 Feb, which is also obvious in Figure 35(a). In February, the marshlands were covered by water and therefore, there was only a slight change in the water borders according to Figure 36(d) and Figure 36(b). This means that the flood started draining and new vegetation was growing instead. In April and May, almost all the flooding water drained from the region and small plants were growing resulting in a large vegetation change in the marshlands, as seen in Figure 36(d) and Figure 36(c). As the next example, we analyse the rice paddy dynamics.

According to Figure 36(a) and (d), from late May to early July, there were significant changes in both datasets. This period is the beginning of the rice plantation season and therefore, according to [20], the vegetation mass increases steeply. However, after these periods, the change in the vegetation mass decreases exponentially until the rice grains become straw. As more grains turn yellow, the change exhibits a quadratic growth until the harvest time, from late September to late October. Figure 37(d–f) and (g–i) visualize the vegetation changes in rice fields between May and August based on the Landsat and Sentinel-2 datasets, respectively. According to Figure 37(d) and (g), some rice paddies experienced a considerable change in May 2010, whereas in May 2016 the whole rice plantation area largely changed. While in June 2010 the changes increased within the rice paddies, in June 2015 the changes slightly decreased, as can be seen in Figure 37I and (h). In both years, the vegetation mass of the rice paddies experienced a gentle change in July [22]-[23], see Figure 37(f) and (i). Additionally, comparing the computed changes in Figure 37, the rice paddies were cultivated more homogeneously in 2015, as the whole area was changing similarly. According to Figure 36(b) and (d), the Landsat dataset shows a significant vegetation mass change in the berry fields in October 2009; however, according to the Sentinel-2 dataset, in 2016 the fields experienced this change in August.

9.2.3.2 Conclusions

In this work, we proposed an approach for land-cover change analysis based on LDA. For our experiments, we used a Landsat and a Sentinel-2 ITS data set of the Doñana National Park. The results show that the changes measured by the proposed approach are able to represent the vegetation dynamics of the study area. Additionally, comparing the results obtained from the two datasets demonstrates that using high-level information allows the proposed approach to measure the changes regardless of the sensor. This will help long-term land cover monitoring by combining various available data. For a future work, one can further analyse the changes measured by the topics based on other spectral indices.

10.   General Conclusion

In this Deliverable, we presented and validated four tools for SAR and multi-spectral ITS images. This was done in two ways: **the first one** by collecting feedback from the partners in the consortium who knows these protected areas very well and **the second one** by submitting the results to well know conferences or journals to be reviewed by the experts in the field.

The goal of the **ITS-DM** tool is to identify similar recurrent patterns into ITS or single images. The validation results were done on Senitnel-2 and Landsat data. The tool was used to generate reference data sets for different areas over the Europe World and not only and were published in [13] and [14]. A more detailed assessment was done in [24] where the results of two SAR sensors (*e.g.,* S-1 and TSX) were compared to each other and for the final interpretation a multi-spectral sensor was also included (S-2). The new development have been published in [13], [14], and [24].

The data mining tool represents the first approach for future ground segments whose functionality will no longer be limited to the mere generation of level 1, 2, or 3 products, but will include automated and user-friendly image content analysis and annotation and also automatic interpretation of SITS together with their statistics.

Regarding the second tool, namely **LDA** the goal is to analyse pairs of images and to identify and to see the evolution of this changes over the time. The results have been presented in [16], [22], and [23].

An approach for land-cover change analysis based on LDA was first time proposed. The dataset used is Landsat and Sentinel-2 SITS of the Donana National Park. The results shows, that the change measured by the proposed approach is able to represent the vegetation dynamics of the study area. Additionally, comparing the results obtained from the two datasets demonstrates that using high-level information allows the proposed approach to measure the changes regardless of the sensor. This will help long-term land-cover monitoring by combining various available data.

The third tool, namely **CoastD** is specific for coastline detection were interested in local changes appearing in sequences of geographically superimposed and co-registered images ideally taken from identical viewpoints. The Polarimetric SAR data was used and the results have been shown in [9].

The method is based on a modified correlation between two different polarimetic amplitude channels (e.g., VV and VH) and the histogram of the correlation map. The histogram is bimodal and can obviously separate between land and sea. Canny edge detector is used to extract the coastline in the binary image obtained by the threshold determined from the histogram. The experiments were run on Sentinal-1A SAR image dataset that cover the Danube Delta which is a protected area included on the UNESCO World Heritage List. The image time series were acquired for a long period. The behaviour of the test site during three months can be summarized as follows: (1) for large water body, such as sea, lakes, and rivers, the coastline detection method can get stable results for image time series; (2) for the vegetation area, like agricultural land and forest, the method can detect obvious changes over the area.

The last tool, namely **DL** aimed at visualisation of ITS, the extraction of land cover temporal patterns change and the evolution of patterns over time based on deep learning and spectral indices. The first results have been described in [33].

It is first time than a long-term satellite image time series data (of 299 scenes ranging from 1999 till 2017) was analyse using deep learning methods with a good accuracy. Using the RNN we are able: to extract intermediate texture features from the time series image patches, to increase the pixel-wise segmentation / classification accuracy, to process image intensity, year and date information simultaneously.

The technology readiness level of the proposed tools is the following: for **ITS-DM** tool the TRL is 4, for **LDA, CoastD,** and **DL tools** the TRL is 3.

11. References

[1] B. S. Manjunath and W. Y. Ma, "Texture features for browsing and retrieval of image data," IEEE Transactions on Pattern Analysis and Machine Intelligence, vol. 18, no. 8, pp. 837–842, Aug. 1996

[2] Chen, J., Shan, S., He, C., Zhao, G., Pietikainen, M., Chen, X. and Gao, W., "WLD: A Robust Local Image Descriptor". IEEE Transactions on Pattern Analysis and Machine Intelligence 32(9), pp. 1705–1720, 2010

[3] CWI, Monetdb Copyright I, Mar 2008-2011, Available from:http://www.monetdb.org/Home

[4] Cui, S., Dumitru, O. and Datcu, M., "Semantic annotation in Earth observation based on active learning", International Journal of Image and Data Fusion pp. 1–23, 2013

[5] P. Blanchart, M. Ferecatu, S. Cui, and M. Datcu, "Pattern retrieval in large image databases using multiscale coarse-to-fine cascaded active learning," Selected Topics in Applied Earth Observations and Remote Sensing, IEEE Journal of, vol. 7, no. 4, pp. 1127–1141, April 2014.

[6] D. Espinoza-Molina and M. Datcu, "Earth-Observation Image Retrieval Based on Content, Semantics, and Metadata," IEEE Transactions on Geoscience and Remote Sensing, vol. 51, no. 11, pp. 5145–5159, Nov. 2013.

[7] David M. Blei, Andrew Y. Ng, and Michael I. Jordan, "Latent Dirichlet Allocation," Journal of Machine Learning Research, vol. 3, pp. 993–1022, 2003.

[8] S. Kullback and R. A. Leibler, "On information and sufficiency," The Annals of Mathematical Statistics, vol. 22, no. 1, pp. 79–86, Mar. 1951.

[9] Ao, D., Dumitru, O., Schwarz, G., and Datcu, M., "Coastline Detection with Time Series of SAR Images", in Proc. of SPIE, September 2017, Warsaw, Poland, accepted.

[10] Nunziata, F., Buono, A., Migliaccio, M. and Benassai G., "Dual-Polarimetric C- and X-Band SAR Data for Coastline Extraction," IEEE Journal of Selected Topics in Applied Earth Observations and Remote Sensing, 9(11), pp. 4921-4928, 2016

[11] Canny, John. "A computational approach to edge detection." IEEE Transactions on Pattern Analysis and Machine Intelligence 6, pp. 679-698, 1986.

[12] Google Earth, Copyright ©, 2017. Available from: http://www.google.com/intl/en_ALL/help/terms_maps.html

[13] C. O. Dumitru, G. Schwarz, and M. Datcu, "Land Cover Semantic Annotation Derived from High-Resolution SAR Images", IEEE Journal of Selected Topics in Applied Earth Observations and Remote Sensing, 9(6), pp. 2215-2232, 2016.

[14] Dumitru, C.O., Schwarz, G., and Datcu, M., "SAR Image Land Cover Datasets for Classification Benchmarking of Temporal Changes ", IEEE Journal of Selected Topics in Applied Earth Observations and Remote Sensing, 11(5), pp. 1571-1592, 2018.

[15] Dumitru C., Schwarz G., Datcu M., "Improved Image Classification by Proper Patch Size Selection: TerraSAR-X vs. Sentinel-1A". In: Proceedings of IWSSIP, Bratislava; 2016. P. 1-4.

[16] Ricardo Díaz-Delgado, David Aragonés, Isabel Afán, and Javier Bustamante, "Long-term monitoring of the flooding regime and hydroperiod of Doñana marshes with Landsat time series (1974–2014)," Remote Sensing, 8(9), 2016.

[17] I. Palomo, B. Martín-López, P. Zorrilla-Miras, D. García Del Amo, and C. Montes, "Deliberative mapping of ecosystem services within and around Doñana National Park (SW Spain) in relation to land use change," Reg. Environ. Chang., vol. 14, no. 1, pp. 237–251, 2014

[18]   F. Garcia-Novo and C. Marín Cabrera, Doñana: Water and Biosphere, Ministry of the Environment, Madrid, Spain, 2006

[19]   Dalberg, "Saving Doñana from danger to prosperity," WWF Analysis, pp. 1–27, September 2016

[20]   "Servidor de imágenes Landsat y productos derivados de Doñana," http://venus.ebd.csic.es/imgs/, Accessed: 2017.

[21]   Y. Yang and S. Newsam, "Bag-of-visual-words and spatial extensions for land-use classification," in Proc. ACM Int. Conf. Adv. GIS, 2010, pp. 270–279.

[22]   D. Espinoza-Molina, R. Bahmanyar, R. Díaz-Delgado, J. Bustamante, and M. Datcu, "Land-cover change detection using local feature descriptors extracted from spectral indices," in Proc. IGARSS, July 2017.

[23]   Espinoza-Molina, Daniela and Bahmanyar, Reza and Datcu, Mihai and Diaz-Delgado, Ricardo, and Bustamante, Javier (2017),"Land-Cover Evolution Class Analysis in Image Time Series of Landsat and Sentinel-2 Based on Latent Dirichlet Allocation", In: Proceeding of MultiTemp, 27-29 Jun 2017, Bruges, Belgium.

[24]   C.O Dumitru, G. Schwarz, D. Espinoza-Molina, M. Datcu, H. Hummel, and C.A. Hummel, "Analysis of Coastal Areas Using SAR Images: A Case Study of the Dutch Wadden Sea Region", book chapter in Topics in Radar Signal Processing, InTech Publishing, Rijeka, Croatia, online May 2018.

[25]   J. Han, M. Kamber, and J. Pei, "Data Mining: Concepts and Techniques", Elsevier Ltd, Oxford, 2011.

[26]   LAST-EBD Remote Sensing and GIS Lab, Estación Biológica de Doñana (CSIC), Avda. Américo Vespucio s/n, Isla de la Cartuja, 41092 Sevilla, Spain

[27]   Y. LeCun, Y. Bengio, G. Hinton, "Deep Learning", Nature, pp. 436-444, Vol. 521, 28 May 2015

[28]   S. Hochreiter, J. Schmidhuber, Long Short Term Memory, Neural Computing, Vol. 9, pp. 1735-1780

[29]   M. Rußwurm, M. Körner, "Multi-Temporal Land Cover Classification with Sequential Recurrent Encoders", ISPRS International Journal of Geoinformatics, 2018, pp. 1-19

[30]   L. Mou, L. Bruzzone, and X. Xiang Zhu, "Learning Spectral-Spatial-Temporal Features via a Recurrent Convolutional Neural Network for Change Detection in Multispectral Imagery", submitted to IEEE TGARS, March 6, 2018

[31]   Product Guide: Landsat Surface Reflectance-Derived Spectral Indices, Department of the interior U.S. geological survey, version 3.6, December 2017

[32]   Understanding LSTM Networks, http://colah.github.io/posts/2015-08-Understanding-LSTMs/

[33]   W. Yao and M. Datcu, "Deep Neural Networks based Semantic Segmentation for Optical Time Series", accepted in IGARSS 2018.

[34]   T. Costachioiu and M. Datcu, "Land Cover Dynamics Classification Using Multi-Temporal Spectral Indices from Satellite Image Time Series," in Proc. COMM, pp. 157-160, 2010.

[35]   T. Costachioiu et al., "Semantic Analysis of Satellite Image Time Series," in Proc. EUSIPCO, pp. 2492-2495, 2012.

[36]   T. Costachioiu et al., "Multitemporal Satellite Image Time Series Analysis of Urban Development in Bucharest and Ilfov Areas," in Proc. COMM, pp. 1-4, 2014.

[37]   D. M. Blei et al., "Latent Dirichlet Allocation," The Journal of Machine Learning Research, vol. 3, pp. 993–1022, Mar. 2003.

[38]   J.S. Lee, and I. Jurkevich, "Coastline Detection and Tracing in SAR Images," IEEE Transactions on Geoscience and Remote Sensing, 28(4), 662-668, 1990.

[39] D.C. Mason, and I.J. Davenport, "Accurate and Efficient Determination of the Shoreline in ERS-1 SAR Images", IEEE Transactions on Geoscience and Remote Sensing, 34(5), 1243-1253, 1996.

[40] A. Niedermeier, E. Romaneeßen, and S. Lehner, "Detection of Coastlines in SAR Images using Wavelet Methods," IEEE Transactions on Geoscience and Remote Sensing, 38(5), 2270-2281, 2000.

[41] C. Liu, J. Yang, J. Yin, and W. An, "Coastline Detection in SAR Images Using a Hierarchical Level Set Segmentation," IEEE Journal of Selected Topics in Applied Earth Observations and Remote Sensing, 9(11), 4908-4920, 2016.

[42] F. Baselice, and G. Ferraioli, "Unsupervised Coastal Line Extraction from SAR Images," IEEE Geoscience and Remote Sensing Letters, 10(6), 1350-1354, 2013.

[43] F. Nunziata, M. Migliaccio, X. Li, X. and X. Ding, "Coastline Extraction Using Dual-Polarimetric COSMO-SkyMed PingPong Mode SAR Data," IEEE Geoscience and Remote Sensing Letters, 11(1), 104-108, 2014.

[44] Z. Liu, F. Li, N. Li, R. Wang, and H. Zhang, "A Novel Region-Merging Approach for Coastline Extraction From Sentinel-1A IW Mode SAR Imagery," IEEE Geoscience and Remote Sensing Letters, 13(3), 324-328, 2016.

[45] M. Rußwurm, and M. Körner, "Multi-Temporal Land Cover Classification with Sequential Recurrent Encoders", ISPRS International Journal of Geoinformatics, pp. 1-19, 2018.

[46] M. Lichao, L. Bruzzone, and X. Zhu, "Learning Spectral-Spatial-Temporal Features via a Recurrent Convolutional Neural Network for Change Detection in Multispectral Imagery", submitted to IEEE TGARS, 2018.